Supporting Information: The mechanism for acetate formation in electrochemical $CO_{(2)}$ reduction on Cu: selectivity with potential, pH, and nanostructuring

Hendrik H. Heenen,[*,†,‡,¶] Haeun Shin,[†,§] Georg Kastlunger,[‡] Sean Overa,[§]
Joseph A. Gauthier,[‖,⊥,#] Feng Jiao,[*,§] and Karen Chan[‡]

†*These authors contributed equally*

‡*Department of Physics, Technical University of Denmark, DK-2800, Kgs. Lyngby, Denmark*

¶*Fritz-Haber-Institut der Max-Planck-Gesellschaft, Faradayweg 4-6, 14195 Berlin, Germany*

§*Center for Catalytic Science and Technology, Department of Chemical and Biomolecular Engineering, University of Delaware, Newark, DE, USA*

‖*SUNCAT Center for Interface Science and Catalysis, Department of Chemical Engineering, Stanford University, Stanford, California 94305, United States*

⊥*SUNCAT Center for Interface Science and Catalysis, SLAC National Accelerator Laboratory, 2575 Sand Hill Road, Menlo Park, California 94025, United States*

#*Present address: Department of Chemical Engineering, Texas Tech University, Lubbock, TX 79409*

E-mail: heenen@fhi.mpg.de; jiao@udel.edu

Contents

S1 Experimental data for acetate selectivity **S-4**

S1.1 Faradaic efficiency for acetate across different experimental studies S-4

S1.2 Measurement data for CORR in a GDE/flow cell set up for Cu-μP at different KOH concentrations S-5

S1.3 Measurement data for CORR in a GDE/flow cell set up for Cu-μP, Cu-50nmP, and Cu-25nmP at different catalyst loadings S-6

S1.4 Electrochemical surface & roughness characterization S-9

S1.5 Loading experiments for CORR in a GDE/flow cell in alkaline conditions . . S-11

S2 Details of DFT calculations **S-16**

S3 Discussion of computed reaction barriers **S-17**

S3.1 Electrochemical barriers for the reduction towards and of H_2CCO^* S-17

S3.2 Reaction barrier for the surface hydrolysis of ketene to acetate S-19

S4 Influence of pH and roughness on Acetate selectivity **S-21**

S5 Coupled microkinetic and transport model **S-21**

S5.1 Details of the microkinetic model S-21

S5.2 Details of the mass transport model S-25

S5.3 Electroneutral Nernst-Planck Approximation S-28

S5.4 Multiscale description of the GDE setup S-30

S5.5 Trends of concentration profiles in the mass transport model S-34

S5.6 Sensitivity of kinetics to energetics S-35

S5.6.1 (Re-)adsorption energy influences SDS-sol S-35

S5.6.2 Barrier competition influences SDS-surf S-36

S5.6.3 Acetate selectivity is insensitive to DFT thermodynamics S-38

S6 The pH dependence of the acetate selectivity necessitates a solution reaction **S-39**

S7 Analytical derivation of acetate selectivity through ketene hydrolysis **S-41**

S7.1 Analytical derivation of diffusion-reaction system for ketene hydrolysis S-41

S7.2 Analytical expression for acetate selectivity S-44

References **S-45**

S1 Experimental data for acetate selectivity

S1.1 Faradaic efficiency for acetate across different experimental studies

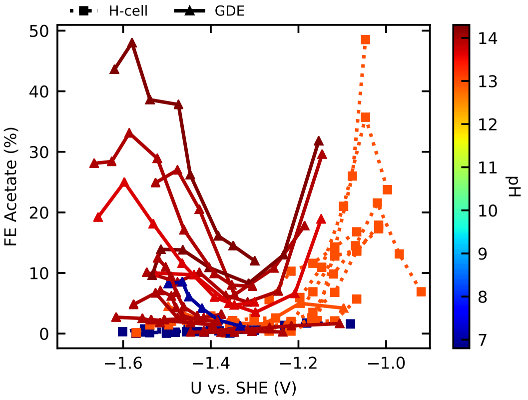

Figure S1: Faradaic efficiency (FE) for acetate against U_{SHE}. Each line represents an individual data set of same reaction conditions and is color-coded according to the electrolyte pH. The data is only adapted for CORR (reduction of CO) measurements from S1–S4. We only included CORR measurements since FEs of acetate are very low at low electrolyte pH usually found in CO_2RR where it is therefore not detected (see main text). The FE for acetate displays a U-shaped profile similar to the selectivity for acetate among the C_2 products (see main text).

S1.2 Measurement data for CORR in a GDE/flow cell set up for Cu-μP at different KOH concentrations

Table S1: Measured data for CORR experiments on Cu-μP (1 μm Cu particles) at different KOH concentrations. Given are the potential U in V vs RHE, the total current density j_{tot} in mA cm^{-2}, and the Faradaic efficiencies for the measured products. The data corresponds to the Cu-μP data in Fig. 4b in the main text.

0.5M KOH (pH=13.7)

		Faradaic efficiency (%)					
U	j_{tot}	H_2	CH_4	C_2H_4	AcO^-	EtOH	PrOH
-0.54 ± 0.00	5.0	31.9 ± 2.7	0.0 ± 0.0	25.1 ± 1.8	5.3 ± 1.7	4.5 ± 0.6	6.5 ± 2.3
-0.61 ± 0.02	10.0	27.0 ± 2.1	0.0 ± 0.0	29.6 ± 2.5	9.7 ± 1.6	11.1 ± 2.2	7.1 ± 2.5
-0.68 ± 0.01	50.0	20.5 ± 3.0	0.8 ± 1.0	25.1 ± 1.8	16.4 ± 3.0	14.6 ± 2.3	4.9 ± 1.4
-0.72 ± 0.00	100.0	17.8 ± 1.3	3.1 ± 1.8	24.5 ± 1.4	21.6 ± 2.7	13.0 ± 1.6	4.4 ± 0.3
-0.74 ± 0.01	200.0	20.5 ± 2.3	8.4 ± 2.3	22.1 ± 1.0	23.5 ± 1.7	9.9 ± 0.1	2.9 ± 0.5
-0.76 ± 0.02	300.0	20.7 ± 1.3	12.4 ± 2.5	18.9 ± 1.0	25.4 ± 2.3	8.3 ± 1.5	2.0 ± 0.5

1.0M KOH (pH=14.0)

		Faradaic efficiency (%)					
U	j_{tot}	H_2	CH_4	C_2H_4	AcO^-	EtOH	PrOH
-0.52 ± 0.01	5.0	31.6 ± 3.5	0.0 ± 0.0	23.6 ± 1.0	7.8 ± 1.8	3.1 ± 1.9	3.2 ± 1.9
-0.57 ± 0.01	10.0	28.7 ± 4.4	0.0 ± 0.0	24.4 ± 2.2	13.2 ± 4.9	10.2 ± 3.3	10.6 ± 1.4
-0.64 ± 0.02	50.0	18.2 ± 0.9	0.0 ± 0.0	23.5 ± 0.6	19.3 ± 1.2	15.1 ± 0.8	5.6 ± 0.5
-0.67 ± 0.02	100.0	18.4 ± 1.9	1.3 ± 2.2	24.3 ± 0.6	21.5 ± 2.4	13.6 ± 1.4	4.1 ± 0.4
-0.69 ± 0.01	200.0	19.1 ± 0.8	3.3 ± 2.7	21.6 ± 1.7	28.9 ± 1.2	10.3 ± 1.7	3.1 ± 0.6
-0.71 ± 0.01	300.0	24.5 ± 2.6	6.9 ± 4.0	18.5 ± 2.1	29.2 ± 6.7	9.7 ± 2.0	1.8 ± 0.8
-0.74 ± 0.00	500.0	25.5 ± 0.0	8.0 ± 0.0	22.1 ± 0.0	29.7 ± 0.0	8.6 ± 0.0	1.2 ± 0.0

2.0M KOH (pH=14.3)

		Faradaic efficiency (%)					
U	j_{tot}	H_2	CH_4	C_2H_4	AcO^-	EtOH	PrOH
-0.50 ± 0.00	5.0	22.2 ± 3.2	0.0 ± 0.0	25.4 ± 1.4	19.7 ± 3.2	4.0 ± 1.3	4.6 ± 4.5
-0.55 ± 0.02	10.0	20.4 ± 1.2	0.0 ± 0.0	27.9 ± 0.3	17.6 ± 3.3	9.8 ± 2.0	4.9 ± 4.5
-0.62 ± 0.01	50.0	15.1 ± 0.2	0.0 ± 0.0	23.5 ± 1.7	28.6 ± 5.6	13.2 ± 2.2	4.1 ± 0.6
-0.64 ± 0.00	100.0	14.7 ± 0.6	0.0 ± 0.0	21.4 ± 2.8	36.3 ± 6.1	12.6 ± 1.2	3.7 ± 0.3
-0.67 ± 0.00	200.0	17.0 ± 1.0	1.8 ± 1.3	19.8 ± 2.0	37.1 ± 4.4	10.1 ± 1.9	2.6 ± 0.3
-0.68 ± 0.00	300.0	20.0 ± 1.4	3.9 ± 1.4	18.6 ± 2.0	35.0 ± 3.6	8.7 ± 1.1	2.0 ± 0.3
-0.70 ± 0.00	500.0	19.4 ± 6.6	8.9 ± 3.0	18.7 ± 2.1	30.9 ± 3.8	8.7 ± 0.9	1.7 ± 0.4

S1.3 Measurement data for CORR in a GDE/flow cell set up for Cu-μP, Cu-50nmP, and Cu-25nmP at different catalyst loadings

Table S2: Measured data for CORR experiments on Cu-μP (1 μm Cu particles) at different catalyst loadings. Given are the potential U in V vs RHE, the total current density j_{tot} in mA cm^{-2}, and the Faradaic efficiencies for the measured products. The data corresponds to the data in Fig. 5b and S4 in the main text and SI, respectively. Note, that in comparison to Cu-50nmP, and Cu-25nmP a low loading of 0.3 mg cm^{-2} was practically difficult to realize due to high overpotentials.

Cu-μP

		Faradaic efficiency (%)					
U	j_{tot}	H_2	CH_4	C_2H_4	AcO^-	EtOH	PrOH
loading = 0.5 mg cm^{-2}							
-0.59	10.0	20.0	0.0	22.1	13.5	11.6	4.6
-0.68	50.0	14.1	0.2	22.9	27.0	20.8	3.1
-0.71	100.0	20.1	9.8	18.5	29.9	15.0	1.9
-0.73	150.0	23.8	18.0	16.4	28.2	12.2	1.5
-0.74	200.0	27.6	23.2	15.2	24.2	9.6	1.3
loading = 1.0 mg cm^{-2}							
-0.52	5.0	31.6	0.0	23.6	7.8	3.1	3.2
-0.57	10.0	28.7	0.0	24.4	13.2	10.2	10.6
-0.64	50.0	18.2	0.0	23.5	19.3	15.1	5.6
-0.67	100.0	18.4	1.3	24.3	21.5	13.6	4.1
-0.69	200.0	19.1	3.3	21.6	28.9	10.3	3.1
-0.71	300.0	24.5	6.9	18.5	29.2	9.7	1.8
-0.74	500.0	25.5	8.0	22.1	29.7	8.6	1.2
loading = 1.5 mg cm^{-2}							
-0.53	10.0	25.2	0.0	27.3	10.4	12.2	14.7
-0.61	50.0	16.1	0.0	28.0	13.9	17.0	5.7
-0.65	100.0	15.9	0.0	26.2	19.7	17.3	4.1
-0.67	200.0	21.7	2.8	21.4	24.4	13.3	2.6
-0.69	300.0	22.9	7.5	18.3	23.8	9.9	1.9
-0.71	500.0	34.6	9.2	12.6	22.1	7.8	1.4

Table S3: Measured data for CORR experiments on Cu-50nmP (40-60 nm Cu particles) at different catalyst loadings. Given are the potential U in V vs RHE, the total current density j_{tot} in mA cm^{-2}, and the Faradaic efficiencies for the measured products. The data corresponds to the data in Fig. S4.

Cu-50nmP

		Faradaic efficiency (%)					
U	j_{tot}	H_2	CH_4	C_2H_4	AcO^-	EtOH	PrOH
loading = 0.3 mg cm^{-2}							
-0.51	10.0	21.1	0.0	29.2	8.5	8.6	12.8
-0.60	50.0	14.0	0.0	31.9	14.1	13.5	9.3
-0.62	100.0	10.8	0.0	31.8	17.8	16.5	7.0
-0.65	200.0	9.6	0.0	31.1	19.9	17.5	4.8
-0.67	400.0	14.1	2.6	30.0	23.8	16.4	3.1
-0.69	600.0	26.1	5.5	25.0	20.1	12.2	2.2
loading = 0.5 mg cm^{-2}							
-0.50	10.0	21.5	0.0	29.6	7.6	8.6	13.8
-0.59	50.0	16.8	0.0	28.7	10.9	12.3	10.8
-0.61	100.0	13.6	0.0	29.9	14.4	15.4	8.9
-0.63	300.0	14.4	0.2	29.0	19.2	20.4	5.2
-0.65	500.0	19.1	2.3	26.3	15.6	14.4	3.8
loading = 1.0 mg cm^{-2}							
-0.46	10.0	21.3	0.0	26.1	6.5	6.7	21.1
-0.54	50.0	17.9	0.0	30.2	8.0	8.3	13.2
-0.56	100.0	15.0	0.0	32.0	11.2	12.3	12.1
-0.58	300.0	14.0	0.0	32.0	15.7	17.2	7.6
-0.61	500.0	17.6	0.7	31.8	18.0	17.6	5.9
-0.63	700.0	28.7	4.0	26.4	16.0	12.8	3.9
loading = 1.5 mg cm^{-2}							
-0.42	10.0	24.7	0.0	20.5	7.1	12.5	18.7
-0.53	50.0	23.1	0.0	26.9	6.2	10.3	14.5
-0.55	100.0	22.2	0.0	28.7	9.5	14.5	13.9
-0.56	200.0	19.3	0.0	29.5	10.3	15.2	8.5
-0.57	300.0	17.9	0.0	29.0	13.4	18.4	7.9
-0.59	500.0	19.1	0.1	29.2	13.5	17.7	5.7

Table S4: Measured data for CORR experiments on Cu-25nmP (25 nm Cu particles) at different catalyst loadings. Given are the potential U in V vs RHE, the total current density j_{tot} in mA cm^{-2}, and the Faradaic efficiencies for the measured products. The data corresponds to the data in Fig. 5b and S4 in the main text and SI, respectively.

Cu-25nmP

		Faradaic efficiency (%)					
U	j_{tot}	H_2	CH_4	C_2H_4	AcO^-	EtOH	PrOH
loading = 0.3 mg cm^{-2}							
-0.50	10.0	21.0	0.0	26.8	9.2	12.1	18.2
-0.59	50.0	14.6	0.0	28.0	13.8	19.0	8.3
-0.62	100.0	11.8	0.0	27.1	17.9	20.8	5.3
-0.64	200.0	23.2	5.7	20.3	20.0	18.5	2.6
-0.67	300.0	33.3	7.9	16.4	17.0	14.4	2.2
loading = 0.5 mg cm^{-2}							
-0.46	10.0	41.2	0.0	15.4	8.7	8.1	13.9
-0.55	50.0	20.8	0.0	21.1	9.6	12.8	15.0
-0.58	100.0	14.2	0.0	24.0	12.1	14.5	11.9
-0.63	300.0	13.5	0.0	29.3	18.2	21.7	8.0
-0.66	500.0	11.2	0.0	33.8	20.4	24.5	6.1
-0.68	700.0	17.8	0.5	32.6	19.8	20.6	4.0
loading = 1.0 mg cm^{-2}							
-0.37	5.0	7.3	0.0	7.3	12.7	8.1	5.2
-0.42	10.0	23.2	0.0	17.4	7.5	8.1	19.1
-0.53	50.0	25.1	0.0	21.4	7.6	9.6	15.8
-0.57	150.0	15.5	0.0	26.2	10.4	15.6	13.9
-0.60	300.0	8.8	0.0	28.1	15.4	17.7	9.8
-0.63	500.0	6.8	0.0	34.2	10.6	24.2	9.9
-0.66	800.0	7.0	0.0	36.6	12.6	25.3	6.1
loading = 1.5 mg cm^{-2}							
-0.40	10.0	15.7	0.0	15.5	9.8	12.1	19.9
-0.49	50.0	18.8	0.0	21.6	7.5	11.2	18.7
-0.54	100.0	17.3	0.0	25.3	9.6	14.5	16.1
-0.58	300.0	10.2	0.0	28.0	14.2	21.6	14.9
-0.61	500.0	8.6	0.0	33.1	13.4	20.9	9.9
-0.64	800.0	6.5	0.0	37.5	10.1	19.5	7.6
-0.66	1000.0	10.0	0.0	42.5	11.4	18.8	6.4

S1.4 Electrochemical surface & roughness characterization

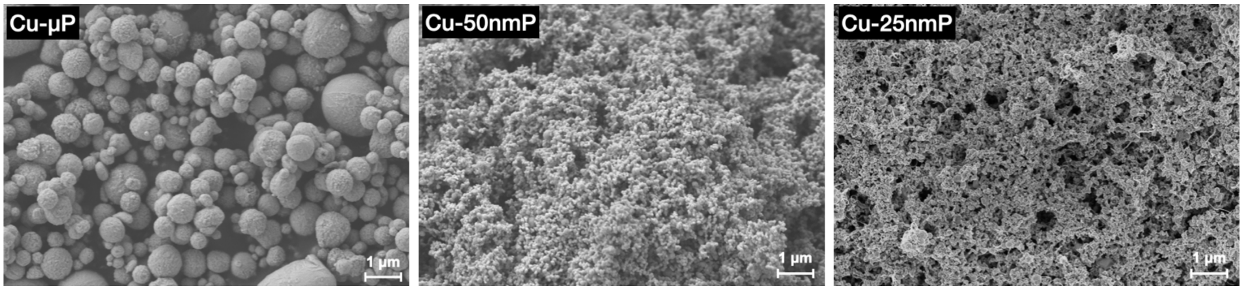

Figure S2: Scanning electron microscope (SEM) images of the commercial Cu-μP (1 μm Cu particles, left), Cu-50nmP (40-60 nm Cu particles, center), and Cu-25nmP (25 nm Cu particles, right) used for the pH and loading experiments, respectively, in this work. It can clearly be seen that Cu-μP diameters are few hundred nm wide while Cu-50nmP and Cu-25nmP show significantly lower diameters. For the characterization of other samples which have been used as comparison in the pH experiments (OD-Cu and Cu-NS) we refer to S1 and S2, respectively.

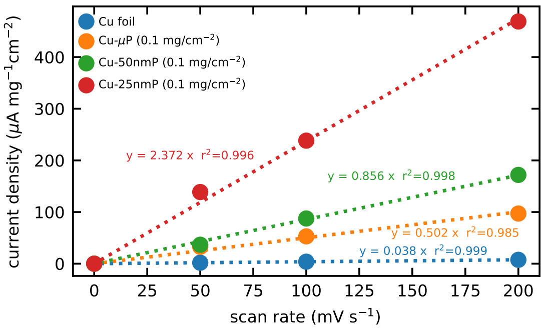

Figure S3: Measurements of the double layer capacitance for Cu-μP (orange), Cu-50nmP (green), and Cu-25nmP (red) dropcast on Toray Paper. The capacitance is determined from cyclic voltammograms (CVs) conducted in an inert gas-purged H-cell. During the CVs, the current density defining the double layer charging is obtained at different scan rates within a potential range where adsorption, desorption or Faradaic processes are absent.

Table S5: Measured specific double layer capacitance C_{dl} and roughness factors R_f for Cu-μP, Cu-50nmP, and Cu-25nmP on Toray paper (Toray). Additionally, to the data measured in this work we show R_f for Cu-NS and OD-Cu used in the pH measurements as taken from S1, S2 measured in a GDE. We also display $\tilde{R}_f$ as the mass loading normalized R_f. R_f was determined in this work on Toray paper which leads to a more reliable estimate. Toray paper is very planar and allows for a more homogeneous distribution of particles where the lower loading on Toray is comparable in particle density to the high surface area GDE substrate. We note that we compared R_f values determined on GDE data which generally lead to similar results which, however, were not well reproducible.

	substrate	loading (mg cm^{-}2)	C_{dl} (μF cm^{-2})	R_f	$\tilde{R}_f$
Cu foil	-	-	37.8	1.0	-
Cu-μP	Toray	0.1	50.18	1.3	13.0
Cu-50nmP	Toray	0.1	85.65	2.3	23
Cu-25nmP	Toray	0.1	237.21	6.3	63
Cu-NS[S2]	GDE	0.5	-	5.0	10.0
OD-Cu[S1]	GDE	1.0	-	65.2	65.2

S1.5 Loading experiments for CORR in a GDE/flow cell in alkaline conditions

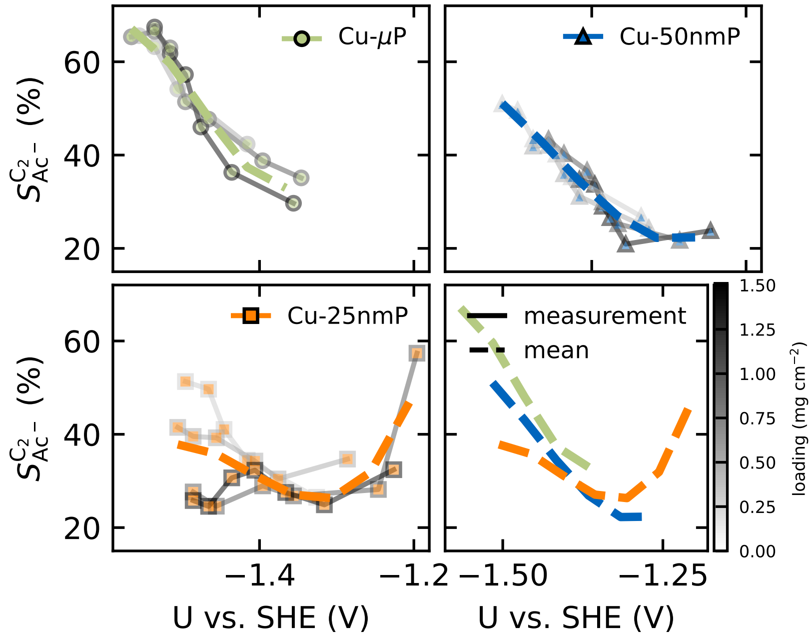

Figure S4: Acetate selectivity among all C_2 products $S^{C_2}_{Ac^-}$ against U_{SHE} obtained from the loading experiments for Cu-μP (top left, green), Cu-50nmP (top right, blue), and Cu-25nmP catalysts (bottom left, orange). The different loadings are color coded as shown in the color bar. The average $S^{C_2}_{Ac^-}$ for each catalyst is shown on the bottom right. The mean $S^{C_2}_{Ac^-}$ reproduces the expected acetate selectivities according to the measured catalyst's roughness (with ρ(Cu-μP) < ρ(Cu-50nmP) < ρ(Cu-25nmP), see Tab. S5). It can be seen that for Cu-μP and Cu-50nmP, $S^{C_2}_{Ac^-}$ is unaffected by the catalyst loading. The selectivities track each other closely. In contrast to this, $S^{C_2}_{Ac^-}$ varies strongly different loadings of Cu-25nmP which becomes very obvious at high overpotentials. High loadings thereby favor other C_2 products which indicates that a high microscopic roughening occurs due to particle overlap. We note, that this roughening on a microscopic length scale is still accompanied by a macroscopically lowered surface area due to the particle overlap (see above Tab. S5). This particle size dependent loading effect agrees with the predicted selectivity influencing microscopic length scales (see main text).

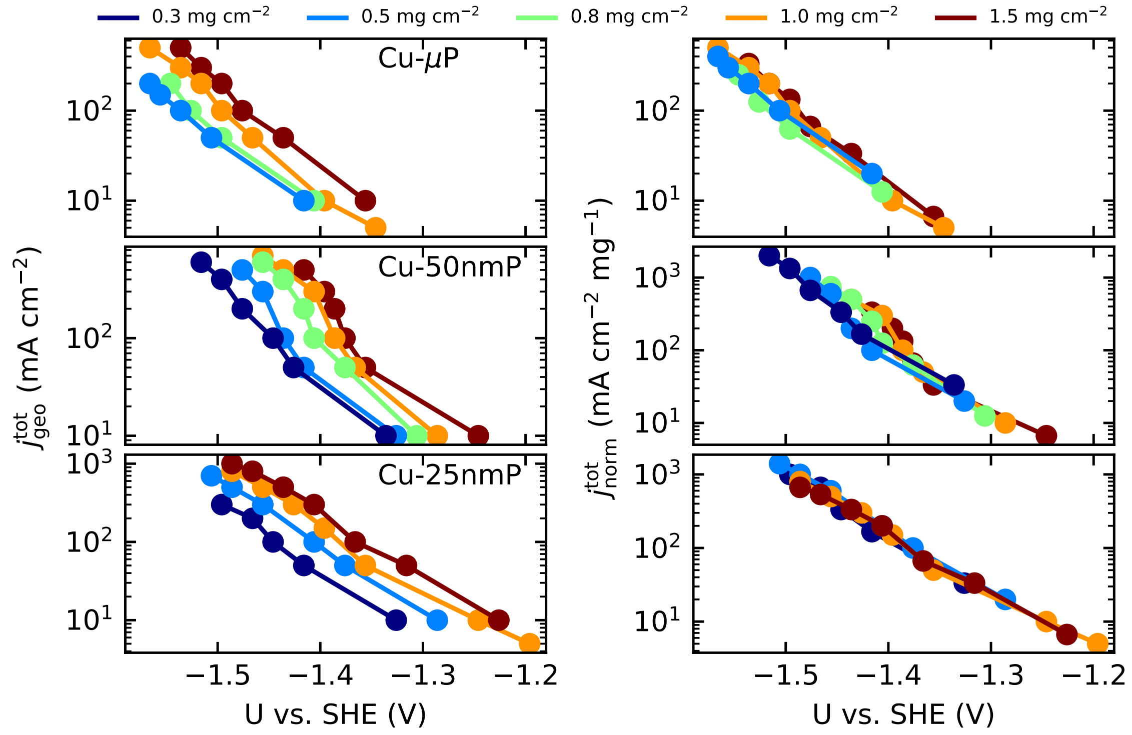

Figure S5: Geometric (left) and mass normalized (right) total current densities against U_{SHE} for Cu-μP (top), Cu-50nmP (center), and Cu-25nmP (bottom) catalysts at different catalyst loadings. The geometric currents obtained from different catalyst loadings overlap after mass normalization which indicates a consistent electrochemical mass activity.

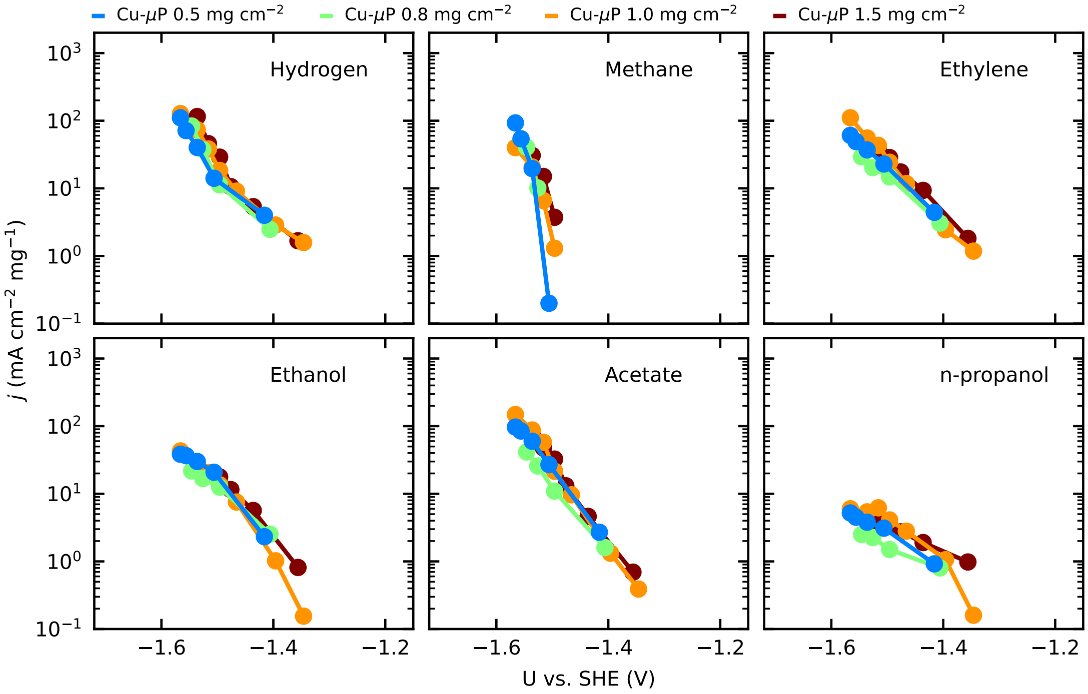

Figure S6: Mass-normalized partial current densities against U_{SHE} for all products measured during the loading experiments for Cu-μP. It can clearly be seen, that the mass-normalized currents of all products overlap with only minor deviation indicating no obvious loading effects on the general product distribution.

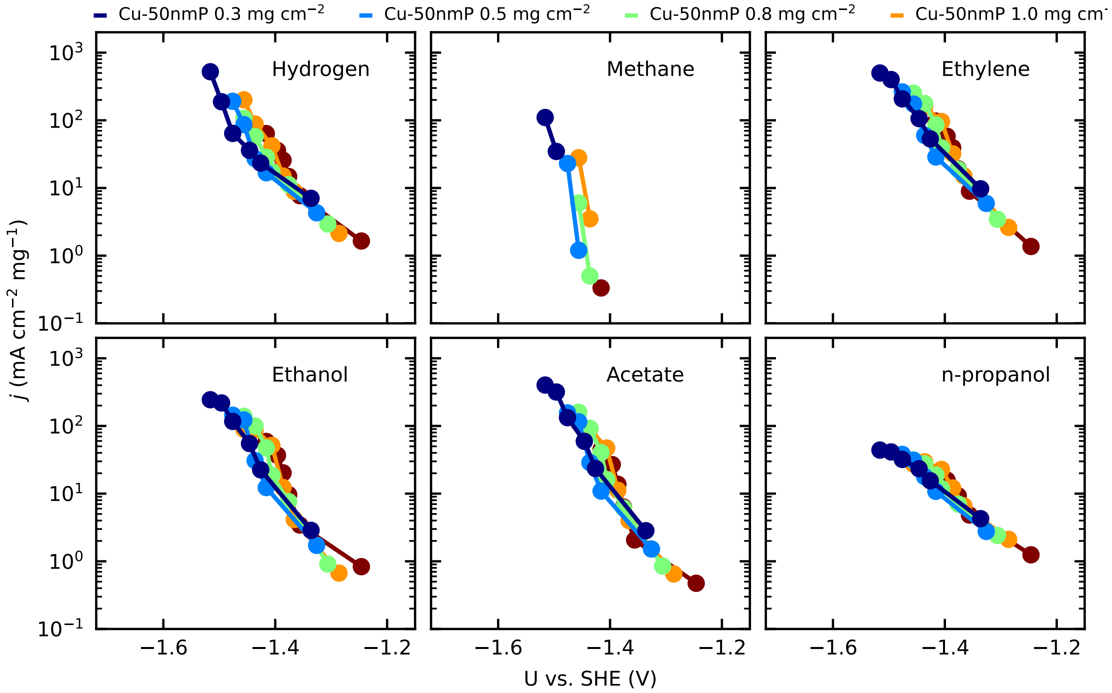

Figure S7: Mass-normalized partial current densities against U_{SHE} for all products measured during the loading experiments for Cu-50nmP. It can clearly be seen, that the mass-normalized currents of all products overlap with only minor deviation indicating no obvious loading effects on the general product distribution.

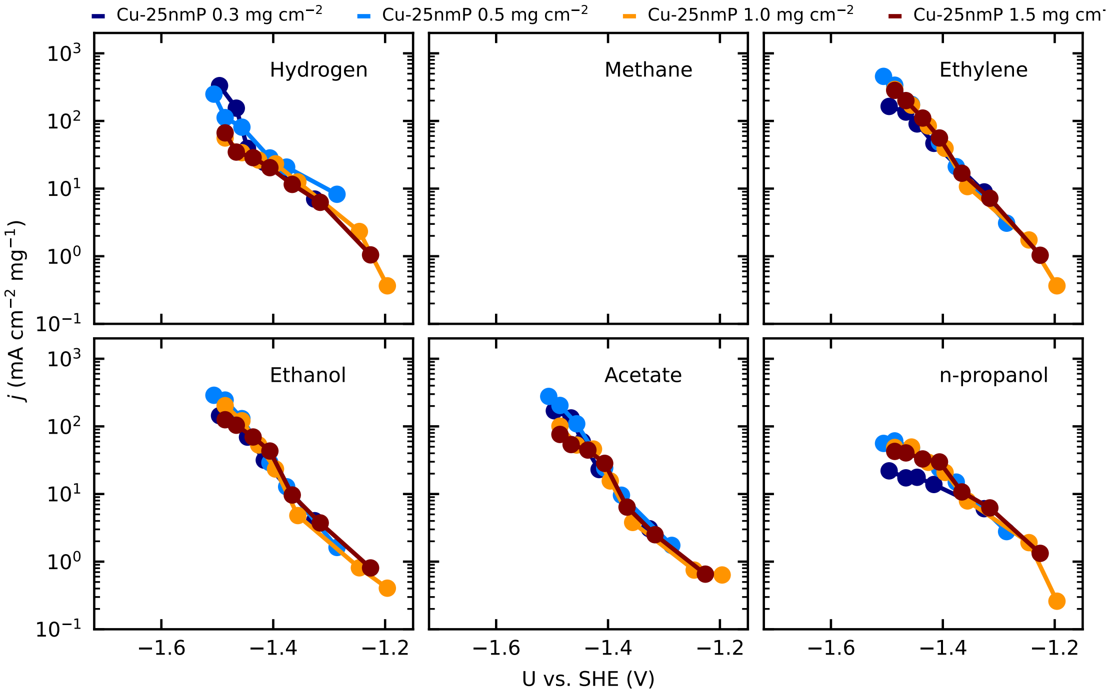

Figure S8: Mass-normalized partial current densities against U_{SHE} for all products measured during the loading experiments for Cu-25nmP. We note, that Methane could not be reliably detected in the setup for Cu-25nmP. The mass-normalized currents of most products overlap with only minor deviation indicating. A stronger deviation is only obvious for acetate and n-propanol.

S2 Details of DFT calculations

All adsorption thermodynamics were computed with GPAW[S5,S6] using the BEEF-vdW[S7] exchange-correlation functional. In GPAW the potential and wave functions are represented on a real space grid with a grid spacing of 0.18 Å and a Fermi temperature of 0.1 K. For the solvated jellium model (SJM), the counter charge starts 3 Å above the explicit atoms, and its thickness has been set to 3 Å. The parameters defining the implicit solvent were chosen in accordance with the optimized values of Held and Walter,[S8] namely $u_0 = 0.18$ eV, $\gamma = 18.4$ dyn cm^{-1}, T = 298 K, $\epsilon_{\text{inf}} = 78.36$. The applied van der Waals radii are based on the determined values of Bondi.[S9] The electronic structure was converged until a total energy difference of 10^{-5} eV. We treated the solid/liquid interface via a hybrid explicit/implicit solvation scheme.[S10] We used the computational hydrogen electrode (CHE) to reference electrochemical reaction thermodynamics.[S11] To mitigate systematic DFT errors of the C=O double bond and the H_2 molecule, we applied the corrections by Christensen *et al.*[S12] We obtained free energies following the ideal gas law for gas phase species and the harmonic oscillator model for adsorbates, respectively.[S13] To obtain the most stable adsorption sites for all surface adsorbates, we conducted a thorough sampling of their symmetrically inequivalent adsorption configurations using the package CatKit.[S14] Geometries were optimized until a force convergence of 0.05 eV/Å. The ketene desorption barriers where calculated via “dynamic” climbing-image nudged-elastic-band (CI-NEB) calculations with a convergence of the forces on the climbing image of 0.05 eV/Å. To represent the different Cu facets, we used slab models with supercells of the sizes 3×4, 4×3, 2×3, and 1×4 and thicknesses of 4, 5, 9, and 4 atom layers for Cu(111), Cu(100), Cu(110), and Cu(211), respectively. We applied a vacuum spacing of 12 Å on each side to avoid interactions across periodic images. The Brillouin zone was sampled via a 4×3×1, 3×4×1, 3×4×1, and 4×3×1 Monkhorst-Pack grid,[S15] respectively. For handling of atomic structures, geometry optimizations, vibration calculations and “dynamic” climbing-image nudged-elastic-band (CI-NEB)[S16] calculations the Atomic Simulation Environment (ASE) package[S17] was used.

The grand canonical PCET barriers where computed using the solvated jellium model (SJM)[S10,S18] as implemented in GPAW[S5,S6] including an explicit water layer and an implicit solvent. H_2O was chosen as the proton donor according to alkaline conditions. We note that the calculations of electrochemical barriers still bear some uncertainties[S19,S20] and only serve as an estimate in this work.

S3 Discussion of computed reaction barriers

S3.1 Electrochemical barriers for the reduction towards and of H_2CCO^*

We investigated the electrochemical barriers for the reduction of $HCCO^*$ and H_2CCO^* on Cu(111), Cu(100), Cu(110), and Cu(211) which constitute the PCET steps around the SDS of acetate. The potential dependence of these barriers is depicted in Fig. S9 and numerical values are given in Tab. S6. The barriers have been computed with an alkaline proton donor (H_2O as donor). We note that we handle these barriers as tentative and only trend-indicating. This is due to the reason that a reliable calculation of electrochemical barriers is still considered challenged due to uncertainties in computational schemes and necessary simplifications of the models.[S19,S20] However, we emphasize that the calculation of alkaline PCET barriers is only made possible by applying a grandcanonical model. This uncertainty is less critical for the computed (chemical) desorption barriers for H_2CCO^* which are also listed in Tab. S6 and discussed below in Sec. S5.6.

For the reduction of $HCCO^*$ we observe that the reaction to $H_2CCO(aq)$, consisting of a simultaneous reduction and desorption, is favored at least at low over potentials on all investigated facets as seen in Fig. S9. This simultaneous process is quite surprising and we hypothesize that it is favored since the direct protonation of the terminal carbon atom is sterically hindered and a desorption of a charged $HCCO^-$ molecule is therefore energetically more feasible. The alternative intermediate $HCCHO^*$ is always less favored

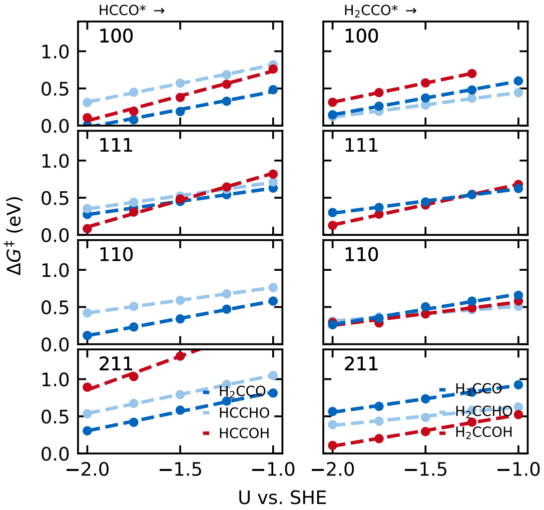

Figure S9: Potential dependence of the free energy barriers computed using SJM[S10] (see methods). Depicted are the barriers for the reduction of the HCCO* (left) and H_2CCO* (right) intermediate with protonation of the terminal C (blue), central C (lightblue), and O (red) on Cu(100), Cu(111), Cu(110), and Cu(211) (from top to bottom).

which is curious as it is actually more stable than H_2CCO* on all facets. The barrier towards this product which involves breaking the C=C=O conjugated double bond system is very high, making this product unlikely. The other alternative intermediate HCCOH* gives an indistinct trend. In the stepped surfaces Cu(110) and Cu(211) the barrier is very high due to an unfavorable HCCOH* intermediate (which spontaneously deprotonates on Cu(110) in presence of explicit water including an OH^-). On the terrace sites Cu(100) and Cu(111) it appears that the barrier to HCCOH* is close to the one of H_2CCO(aq). Due to a higher charge transfer coefficient the reduction barrier to HCCOH* stabilizes faster with potential which leads to HCCOH* becoming more probable than H_2CCO(aq) at very high potentials. From our simulations we cannot determine at what potential this competition leads to relevant divergence from the ketene pathway. As discussed in the main text, this competition is, however, most likely only relevant at very high potentials where ethylene appears to decouple from acetate and ethanol. We note, that this effect is likely facet dependent.[S21,S22]

The reduction of H_2CCO* shows very different trends on the different facets. We find

Table S6: Free energy barriers computed for this work in eV. The adsorption and desorption barriers of H_2CCO ($\Delta G^{\ddagger}_{\mathrm{H_2CCO(aq) \rightarrow H_2CCO^*}}$ and $\Delta G^{\ddagger}_{\mathrm{H_2CCO^* \rightarrow H_2CCO(aq)}}$) have been computed without potential dependence. All other barriers have been computed using SJM[S10] (see methods) and values of $\Delta G^{\ddagger}_{X}$ are shown for -1.32 V vs. SHE (-0.5 V vs. RHE at pH=14).

	Cu(100)	Cu(111)	Cu(110)	Cu(211)
$\Delta G^{\ddagger}_{\mathrm{H_2CCO(aq) \rightarrow H_2CCO^*}}$	0.77	1.05	1.00	0.52
$\Delta G^{\ddagger}_{\mathrm{H_2CCO^* \rightarrow H_2CCO(aq)}}$	0.36	0.20	0.37	0.21
$\Delta G^{\ddagger}_{\mathrm{HCCO^* \rightarrow H_2CCO(aq)}}$	0.30	0.52	0.43	0.66
$\Delta G^{\ddagger}_{\mathrm{HCCO^* \rightarrow HCCHO^*}}$	0.66	0.59	0.65	0.89
$\Delta G^{\ddagger}_{\mathrm{HCCO^* \rightarrow HCCOH^*}}$	0.52	0.60	-	1.47
$\Delta G^{\ddagger}_{\mathrm{H_2CCO^* \rightarrow H_3CCO^*}}$	0.45	0.51	0.54	0.80
$\Delta G^{\ddagger}_{\mathrm{H_2CCO^* \rightarrow H_2CCHO^*}}$	0.34	-	0.45	0.55
$\Delta G^{\ddagger}_{\mathrm{H_2CCO^* \rightarrow H_2CCOH^*}}$	0.67	0.50	0.47	0.39

Cu(100) to favor H_2CCHO^* and H_3CCO, Cu(111) to favor H_3CCO^* and H_2CCOH^*, Cu(110) all possible PCET steps almost equally and Cu(211) to clearly favor H_2CCOH^* (see Fig. S9).

The most likely reduction reactions on the different facets show a β close to 0.5 (0.45-0.52) with the exception of Cu(111) where a β of 0.33 for $HCCO^* \rightarrow H_2CCO(aq)$ is found. In our microkinetic model (see Sec. S5.1) where we employ Cu(100) energetics we therefore use an effective *beta* of 0.5 due to the possible uncertainty in the detailed *beta*s from our constant potential simulations.

S3.2 Reaction barrier for the surface hydrolysis of ketene to acetate

As further discussed in the main text we assume that the OH^- catalyzed hydrolysis of ketene to acetate occurs in solution. Alternatively, this step could be imagined to occur on the electrode surface. However, OH^- would need to perform a nucleophilic attack on H_2CCO while the electrode surface is negatively charged / at negative potentials. This reaction *could* then only occur as a chemical step since electrochemically, it would be an oxidation.

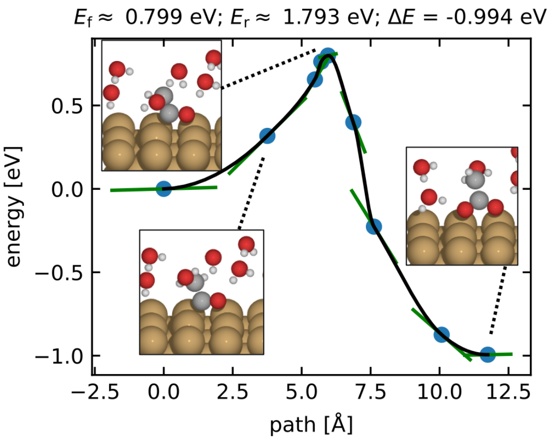

Figure S10: CI-NEB band for the surface hydrolysis of adsorbed ketene (H_2CCO) at -1.5 V vs. SHE. The band depicts the latter part of the complex hydrolysis step (see text) where OH^- adds to H_3CCO^* and gets deprotonated. Shown are the electronic energies as found during the CI-NEB search.

To estimate the feasibility of this reaction we perform a CI-NEB calculation on Cu(100). We apply an external potential at -1.5 V vs. SHE to stabilize the OH^- molecule in our simulation cell. From our CI-NEB search we find the reaction to occur in two steps. Firstly, H_2CCO^* gets reduced to H_3CCO^* where H_3CCO^* forms a stable intermediate (two OH^- then remain in the simulation cell). Secondly, OH^- reacts with H_3CCO^* to acetic acid followed by a deprotonation to form acetate. Analyzing the transferred charge during the reactions, we find the two steps to consist of a reduction followed by two oxidations, formally this reaction therefore does not represent a chemical step. The second step is energetically more difficult and is depicted in Fig. S10. It can be seen that the associated barrier is at 0.79 eV and we find the free energy barrier to be 0.81 eV. This is similarly high as found for $OH^- + CCO^* \rightarrow CCOH^-$.[S23] While this reaction barrier is clearly higher than the solution reaction[S24] (the experimental rate translates to $\Delta G^\ddagger = 0.48$ eV) or other reduction steps (see Fig. S9), a value of 0.8 eV would not lead to an observable reaction rate.[S13]

S4 Influence of pH and roughness on Acetate selectivity

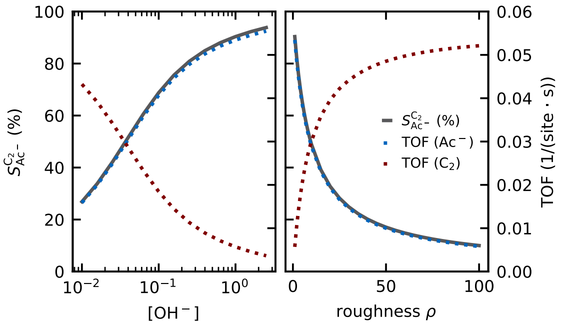

Figure S11: Acetate selectivity among C_2 products ($S^{C_2}_{Ac^-}$) and turn-over-frequencies (TOFs) of acetate (Ac^-) and other C_2 products against OH^- concentration with $\rho = 1$ (left) and against roughness at pH= 14 (right). The relation depicts the transport related acetate selectivity as obtain through our transport coupled microkinetic model. The simulated data corresponds to the conditions met at the minimum of the U-shaped selectivity-potential relationship at U_{SHE} = -1.3 V and the behavior according to Equ. 1 in the main text.

S5 Coupled microkinetic and transport model

S5.1 Details of the microkinetic model

The employed microkinetic model depicts the atomic reactions on the catalyst surface leading to acetate and other C_2 products summarized in Fig. S12 and Fig. 2a in the main text. As described in the main text and in Sec. S6, we assume a shared RDS between acetate and the other C_2 products. We do not include HER and C_1 products since we only aim to describe the selectivity within the ketene pathway (see main text).

We use an effective model to represent the reaction network of the ketene pathway. This model reduces out all steps which are redundant for the selectivity mechanism. The final reaction network is given by the following equations

$$\mathrm{CO(g)} + * \rightleftharpoons \mathrm{CO}^* \tag{1}$$

$$2\mathrm{CO}^* + 2\mathrm{H_2O} + 3\mathrm{e}^- + * \rightleftharpoons \mathrm{HCCO}^* + 3\mathrm{OH}^- \tag{2}$$

$$\mathrm{HCCO}^* + \mathrm{H_2O} + \mathrm{e}^- \rightleftharpoons \mathrm{H_2CCO(aq)} + \mathrm{OH}^- \tag{3}$$

$$\mathrm{H_2CCO(aq)} \rightleftharpoons \mathrm{H_2CCO}^* \tag{4}$$

$$\mathrm{H_2CCO}^* + \mathrm{H_2O} + \mathrm{e}^- \rightleftharpoons \mathrm{H_2CCHO}^* + \mathrm{OH}^- \tag{5}$$

$$\mathrm{H_2CCHO}^* + 4\mathrm{H_2O} + 4\mathrm{e}^- \rightarrow \mathrm{otherC_2(g)} + 4\mathrm{OH}^- \tag{6}$$

Note that the same results are obtained when more steps are included into this effective model. All omitted steps are bundled in Equ. 2. Here, we use a barrier according to the RDS and only the subsequent intermediates OCCO^* and OCCOH^* are left out. When included, these intermediates will establish negligible surface coverages since they follow the RDS with exergonic reaction thermodynamics because we did not include their electrochemical barriers. Omitting these intermediates is therefore without consequence in our model.

The activities of the reactant CO(g) in Equ. 1 and the intermediate $\mathrm{H_2CCO(aq)}$ in Equ. and are not chosen as constant values but influenced by the mass transport models (see below Sec. S5.2). The CO(g) activity depends on the diffusion of CO in the electrolyte towards the catalyst surface which reduces its immediate surface concentration – an effect describing typical mass transport limitations of reactants[S25,S26] (see Sec. S5.4 and main text). The $\mathrm{H_2CCO(aq)}$ activity affects the selectivity between acetate and the other $\mathrm{C_2}$ products. An effective equilibrium between $\mathrm{H_2CCO(aq)}$ and $\mathrm{H_2CCO}^*$ establishes (Equ. S5.1, S5.1, and S5.1), which depends on the concentration of $\mathrm{H_2CCO(aq)}$. The latter is determined by the mass transport model (see below Sec. S5.2). In the reaction towards other $\mathrm{C_2}$ in Equ. 6 we do not consider a back reaction (activity other $\mathrm{C_2(g)} = 0$) since these products are considered fully reduced.

We solve the system of time dependent coupled differential equations 1-6 for the steady-state condition $\frac{d\theta_i}{dt} = 0$, where θ_i is coverage of species i, via a mean field approach using an ODE solver as available in Scipy.[S27] The rate constants k_{ji} for each elementary process are given by the Arrhenius equation $k_{ij} = Ae^{-\frac{\Delta G_a^{ij}}{k_B T}}$. Here, ΔG_a represents the activation energy, k_B the Boltzmann constant, T the temperature, and the prefactor is $A = k_B T/\hbar = 10^{-13}$ s^{-1}.

For the free energies ΔG_a we used the data we computed for the Cu(100) facet via our DFT simulations (see Fig. S12 and main text Fig. 3). We note, however, that the general kinetics are insensitive to the overall used energetics (see Sec. S5.6.3). An only exception is the RDS as well as the desorption equilibrium of ketene and its reduction barrier. For this work we fitted the RDS to the experimental ECSA normalized C_2 activity at low overpotentials from S2. The effective free energy barrier was 1.45 eV at 0 V vs. SHE. With a symmetry factor β of 0.5 the C_2 products have thereby experimental activity, follow a Tafel slope of 119 mV/dec and are independent of pH on the SHE scale reproducing experimental observations.[S2,S28] The effective RDS then corresponds to a model as depicted in Fig. S12. Note, that the fitted RDS includes the CO solubility (hence its concentration in solution) and therefore the coupled mass transport relations (see below Sec. S5.2) scale the effective CO activity. In the employed Cu(100) energetics we need to apply a correction for the solvated ketene to reproduce the experimental behavior as further described in Sec. S5.6.1 and S5.6.2.

We ignored lateral interactions. As shown in Sec. S5.6.3, the Cu(100) energetics used in our model lead to a CO* coverage of 0.25 ML which is a typical value when considering lateral interactions.[S30] Exchanging the reaction free energies only leads to a variation in the surface coverage of *CO for which a interaction model would then be necessary. Otherwise, all other intermediates always show negligible surface coverages and are therefore not subject to lateral interactions. Thus, an interaction model "regulating" the CO* coverage is not necessary in our model.

The dependence of the reaction thermodynamics on applied potential and pH were de-

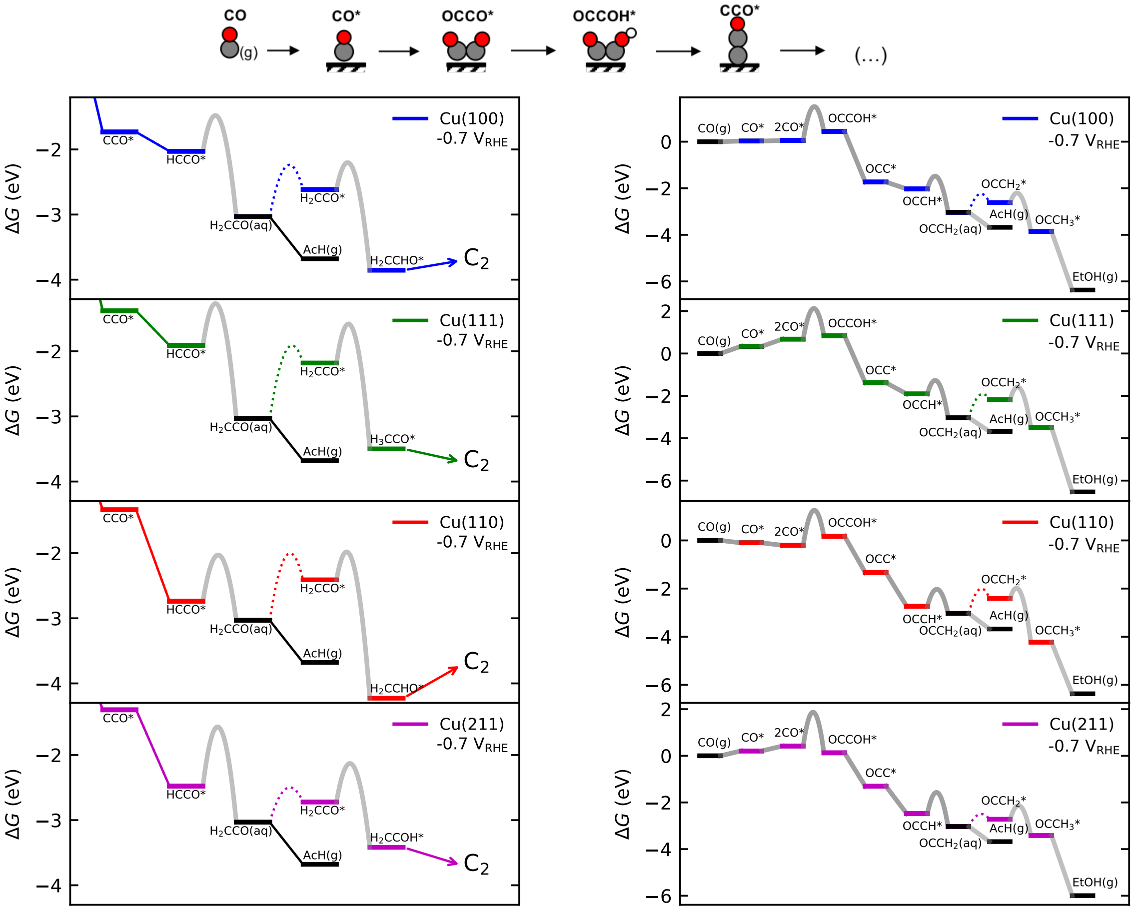

Figure S12: (top) Schematic of the atomic mechanism for C_2 products around the RDS. (bottom) Free energy diagrams for the suggested ketene pathway around the SDS (left) and the complete mechanism (right) on Cu(100), Cu(111), Cu(110), and Cu(211) at -0.7 V vs. RHE (pH=14). Depicted is the considered division into the pathways including reduction of H2CCO* (colored) and the (facet independent) desorption of ketene and its hydrolysis to acetate (black), respectively. The adsorption barrier of ketene (dotted) and the approximated electrochemical barriers (gray, see methods) are shown. Note that we use an effective/fitted RDS (first barrier = 1.45 eV) in the microkinetic model reflecting a behavior following an RDS consisting of the protonation of the OCCO* intermediate or its dimerization following Liu *et al.*[S29] termined with the computational hydrogen electrode (CHE).[S11] The potential dependence of the transition states, was assumed to be linear with a symmetry factor of β which was universally chosen as 0.5. We note that the βs obtained from our constant potential calculations (see Fig. S9) were around 0.5 (0.44-0.52) for the most probable barriers, which agrees with our universally chosen value. An only exception was Cu(111) where a β of 0.33 for $HCCO^* \rightarrow H_2CCO(aq)$ was found (in the microkinetic model we use, however, Cu(100) data).

The microkinetic model yields rates corresponding to the turn-over-frequency (TOF) of an individual catalytic site. We convert these TOFs to molar fluxes using a site-density corresponding to the unit cell of the Cu(100) facet (i.e. every Cu surface atom is a catalytic site).

S5.2 Details of the mass transport model

We explicitly treat the mass transport of CO, OH^- and H_2CCO while assuming a constant activity for H_2O (no depletion) and no transport limitations for the diffusion of other C_2 products (no further reaction possible). To describe the mass transport we use a one dimensional (1-D) transport model. While a 1-D model is a crass simplification of the complex geometry in nanostructured electrodes, it usually covers most of the relevant behavior.[S31] The transport of species is described by the simplified Nernst-Planck (NP) equation:[S32]

$$\frac{dc}{dt} = -\frac{d}{dx}\left[D\frac{dc}{dx} - D\frac{z_i}{k_B T}c(\frac{d\phi}{dx})\right] \tag{7}$$

where c is the concentration, D the diffusion coefficient, z_i the charge of a charged species, ϕ the potential, x the distance, t the time, k_B the Boltzmann constant, and T the temperature. The second term $D\frac{q}{k_B T}c(\frac{d\phi}{dx})$ represents the migration which affects only charged species and drops out in uncharged species. In our case the only charged species is OH^- (and the counter ion, i.e. K^+). Usually, it is necessary to solve the Poisson equation to incorporate migration.

We circumvent this by using an electro-neutral approximation allowing for the analytical solution in Equ. 9 (see Sec. S5.3 for derivation).[S32–S34] This analytical solution leads to an almost equivalent result as the full numeric Poisson-NP equation with the exception of the charge separation at the electrode interface describing the electrochemical double layer. The double-layer related concentration drop at the electrode surface has, however, only marginal influence on transport as further elaborated in Sec. S5.3. The resulting equations governing the transport of CO, OH^- and H_2CCO follow as

$$\frac{d[\mathrm{CO}]}{dt} = -D_{\mathrm{CO}} \frac{d^2[\mathrm{CO}]}{dx^2} \tag{8}$$

$$\frac{d[\mathrm{OH}^-]}{dt} = -2 \cdot D_{\mathrm{OH}^-} \frac{d^2[\mathrm{OH}^-]}{dx^2} - k_{\mathrm{sol}}[\mathrm{OH}^-][\mathrm{H_2CCO}] \tag{9}$$

$$\frac{d[\mathrm{H_2CCO}]}{dt} = -D_{\mathrm{H_2CCO}} \frac{d^2[\mathrm{H_2CCO}]}{dx^2} - k_{\mathrm{sol}}[\mathrm{OH}^-][\mathrm{H_2CCO}] \tag{10}$$

where $[X]$ is the concentration and D_X the diffusion coefficient of species X. The last terms in Equ. 9 and 10 represent the solution reaction between OH^- and H_2CCO to form acetate where k_{sol} is the reaction constant of the solution reaction. The transport of acetate after the solution reaction is ignored since it cannot further react. The factor 2 in Equ. 9 derives from the electro-neutral approximation of the Nernst-Planck equation (see SI Sec. S5.3). For the diffusion coefficients we used $D_{\mathrm{CO}} = 20.3 \cdot 10^{-10}\mathrm{m}^2/\mathrm{s}$,[S35] $D_{\mathrm{OH}^-} = 52.7 \cdot 10^{-10}\mathrm{m}^2/\mathrm{s}$,[S36] $D_{\mathrm{H_2CCO}} = 14.0224 \cdot 10^{-10}\mathrm{m}^2/\mathrm{s}$[S37] and for the solution reaction the experimental value of $k_{\mathrm{sol}} = 5.26 \cdot 10^4\,\mathrm{l}/(\mathrm{mol} \cdot \mathrm{s})$.[S24] We do not apply any corrections to diffusion coefficients due to porosity or tortuosity as is common practice[S32,S36,S38,S39] since no such values can reliably estimated. We note, however, that within typical porosity values the selectivity profile only changes slightly, then showing more agreement with experiment (lower minimum for all ρ).

We use Diriclet boundary conditions on the solution side, with the bulk concentrations of CO, OH, and ketene according to the Henry constant of CO,[S40] the electrolyte pH at the GDE and zero (all ketene reacts to Acetate), respectively. On the catalyst side we use Neumann boundary conditions based on the species flux f corresponding to the CO consumption ($f(\mathrm{CO}) = f(\mathrm{H_2CCO}) + f(\mathrm{other C_2})$), $\mathrm{OH^-}$ production ($f(\mathrm{OH^-}) = 4 \cdot f(\mathrm{H_2CCO}) + 8 \cdot f(\mathrm{other C_2})$) and acetate production ($f(\mathrm{H_2CCO}) = \int_0^\infty f(\mathrm{Ac^-})dx = \int_0^\infty [\mathrm{H_2CCO}][\mathrm{OH^-}]k_{\mathrm{sol}}dx$). When coupling the microkinetic model to the transport, the roughness ρ is used to scale the site dependent activity (TOF) to the molar flux as $f = \rho \cdot \mathrm{TOF}/(N_\mathrm{A} \cdot A_\mathrm{site})$ where N_A is Avogadro's constant and A_site the area per active site (= Cu(100) site density).

We solve all transport equations for the steady-state to mimic the steady currents reached in GDE setups. The diffusion of CO (Equ. 8) is treated independently as described in Sec. S5.4 and therefore solved analytically using Fick's first law. The transport of $\mathrm{OH^-}$ and $\mathrm{H_2CCO}$ is solved numerically using a finite difference scheme with a constant step width of 50 nm and a timestep of 0.3 μs.

We consider the influence of convection of the electrolyte in a flow cell.[S25,S41] For this influence we use a mass transport formalism where the transport f_X^e of a species X perpendicular to the convection is described by[S35]

$$f_X^e = k_X^e(c_X^{\mathrm{surf}} - c_X^{\mathrm{bulk}}). \tag{11}$$

The effective transport coefficient k_X^e is the given by the dimensionless Sherwood number adjusted to the average mass-transport between a planar surface and a laminar flowing liquid with a plate length L_c[S35]

$$Sh = \frac{k_X^e \cdot L_c}{D_X} = 0.646\,(ReSc)^{1/3} \tag{12}$$

where the dimensionless Reynolds (Re) and Schmidt (Sc) numbers are given by

$$Re = \frac{\rho \nu L_c}{\mu} \quad Sc = \frac{\mu}{\rho D_X}. \tag{13}$$

where ρ is the density, μ the dynamic viscosity, and ν the flow velocity of the electrolyte. We note that while the choice of the Sherwood relation affects the local pH quantitatively, alternative formulations like the "Graetz-Nusselt-Problem" in a circular channel geometry give very similar results as Equ. 12 and differences are rather small. The chosen formalism corresponds to the mass transport of dilute solutes which may not be true for OH^-, but usually still presents a good approximation.[S35,S42]

S5.3 Electroneutral Nernst-Planck Approximation

To include migration into our mass transport model we use the electroneutral Nernst-Planck (ENNP) approximation. Migration affects charged species which includes only OH^- (and a counter ion, i.e. K^+) in our model. To treat the transport of a charged species we use the steady-state form of the simplified Nernst-Planck (NP) equation (Equ. 7).[S32] For OH^- and K^+ it would follow

$$j_{\mathrm{OH}^-} = -\left[D_{\mathrm{OH}^-}\frac{d[\mathrm{OH}^-]}{dx} - D_{\mathrm{OH}^-}\frac{e}{k_BT}[\mathrm{OH}^-](\frac{d\phi}{dx})\right] \tag{14}$$

$$j_{\mathrm{K}^+} = -\left[D_{\mathrm{K}^+}\frac{d[\mathrm{K}^+]}{dx} + D_{\mathrm{K}^+}\frac{e}{k_BT}[\mathrm{K}^+]\left(\frac{d\phi}{dx}\right)\right] \tag{15}$$

where j_X is the flux, $[X]$ is the concentration, D_X the diffusion coefficient of $X = \mathrm{OH}^-$ and K^+, x the distance, e the elementary charge, k_B the Boltzmann constant, and T the temperature. To solve for the potential ϕ, we require a third relation.

A full solution to Equ. 14 and 15 and the potential ϕ could be obtained by using Poisson's equation

$$\frac{d}{dx}(\epsilon_0\epsilon_r\frac{d\phi}{dx}) = -\sum_X z_X[X] \tag{16}$$

where ϵ_0 and ϵ_r are the vacuum and relative permittivity, respectively and z the charge. The coupled system of equations is called the Poisson-NP solution (PNP) and can (with few exceptions) only be solved numerically.[S32]

Alternatively to the PNP solution we can instead use a quasi charge neutral condition[S33,S34]

$$\sum_X z_X[X] = 0 \tag{17}$$

which states that all charge is neutralized (no charge separation). We can derive an analytical solution from the coupled migration of the charged species OH^- and K^+.[S32] For this we exploit the fact, that K^+ has no effective flux (not produced at catalyst, $j_{K^+} = 0$) which leads to

$$0 = -\left[D_{K^+}\frac{d[K^+]}{dx} + D_{K^+}\frac{e}{k_B T}[K^+]\left(\frac{d\phi}{dx}\right)\right] \tag{18}$$

we can rearrange and divide by D_{K^+} to obtain

$$\frac{d\phi}{dx} = -\frac{d[K^+]}{dx}\frac{1}{[K^+]}\frac{k_B T}{e} \tag{19}$$

which leaves us with an expression for the field $\frac{d\phi}{dx}$ which we insert into Equ. 14 and simplify to

$$j_{OH^-} = -D_{OH^-}\left[\frac{d[OH^-]}{dx} + \frac{[OH^-]}{[K^+]}\frac{d[K^+]}{dx}\right] \tag{20}$$

based on the charge neutrality criterion the concentrations of ions align with $[OH^-] = [K^+]$ and $\frac{d[OH^-]}{dx} = \frac{d[K^+]}{dx}$ leaving us finally with

$$j_{OH^-} = -2 \cdot D_{OH^-}\frac{d[OH^-]}{dx} \tag{21}$$

The final expression is identical to the steady state diffusion flux (Fick's first law) with an additional factor 2. As shown in Fig. S13, this trivial solution almost perfectly reproduces the much more complex PNP solution. The only difference can be seen within few Å from the catalyst surface. This deviation originates in the electrostatic repulsion of anions and attraction of cation at the negatively charged surface forming the electrochemical double layer. This very relevant phenomenon describing very strong interfacial fields at the metal/water interface cannot be found in the ENNP approximation as charge separation is not included.

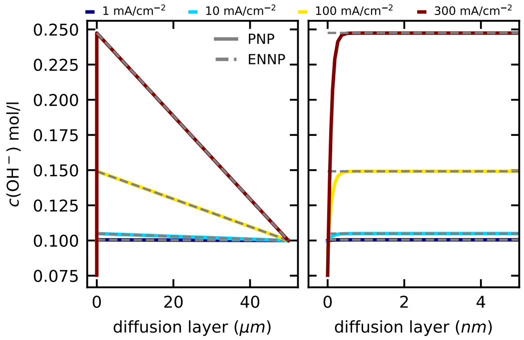

Figure S13: Steady-state concentration profile of OH$^-$ against the surface normal of the catalyst x at different current densities including migration. The solid lines are the numerical solution to the full PNP approach (solved with COMSOL Multiphysics® software[S43]) and dashed lines the corresponding analytical solution using an ENNP approach. The right panel depict an insert showing the concentration profiles few nanometers from the catalyst surface.

The concentration gradients are, however, only affected at a very short range of the catalyst surface and therefore do not affect transport properties.[S33] This is also true for other electrolyte compositions, for example the carbonate buffer equilibrium where charge separation also only extend < 20 Å.[S36] We note, that we use the final result in Equ. 21 and its analogy to the Fick's law of diffusion in Equ. 14 of our mass transport model. The steady-state equilibrium condition is thereby considered for the infinitesimal flux between different elements in our finite difference solver.[S33]

S5.4 Multiscale description of the GDE setup

We merge the microkinetic model (see Sec. S5.1) and the mass transport model following a multi-scale methodology to mimic the conditions in a GDE/flow cell setup as depicted in Fig. S14. Here, the microkinetic model represents the CORR reduction reactions on the catalyst surface (Fig. S14a) while the mass transport equations 8, 9, and 10 represent the diffusion as well as the solution reaction within the electrode (Fig. S14b) and the effective mass transport Sherwood relation (Equ. 11 and 12) represents the transport in the flowing electrolyte (Fig. S14c) to the electrode. In a GDE, gaseous reactants and products are transported through a gas diffusion layer (GDL) which allows for an exchange with the electrolyte in close proximity to the catalyst located at the microporous layer (MPL) as depicted in Fig. S14 b and c. In contrast, the liquid species exchange with the electrolyte "bulk" which is cycled in a flow cell setup.[S25,S26,S41]

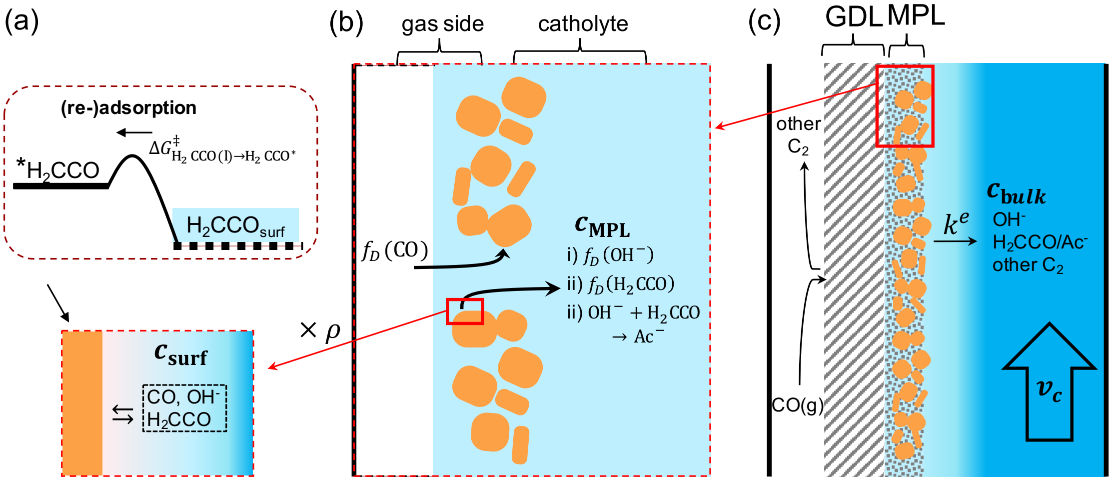

Figure S14: Schematic of the mass transport we describe with our model. (a) Adsorption and desorption processes of the reactant CO and the products OH^- and H_2CCO at the catalyst surface scaling with the roughness ρ and determined by the surface concentration c_{surf}. The governing process for the selectivity of Ac^- is the (re-)adsorption of H_2CCO dependent on the adsorption barrier $\Delta G^{\ddagger}_{H_2CCO(l) \to H_2CCO^*}$. (b) Transport processes occurring within the GDE: diffusion $f_D(X)$ of species X and the solution reaction of OH^- and H_2CCO. All transport processes are dependent on the concentration just outside of the electrode c_{MPL} (c) Processes occurring on cell level: CO and gaseous products (other C_2) exchange through the gas side, while OH^-, H_2CCO, Ac^-, and liquid products (other C_2) exchange with the catholyte. The indicated convection v_c influences the mass transport between the catholyte bulk c_{bulk} and the electrode surface c_{MPL}.

Following the GDE setup we consider the transport of CO on the gas side separately from OH^- and H_2CCO on the electrolyte side (see Fig. S14 b, c). As a consequence, CO does not interact with and has a different diffusion length than OH^- and H_2CCO. Over the GDL, CO only needs to diffuse over an unknown short diffusion length which significantly improves the mass transport. In our 1D model we need to assume a gas side diffusion layer thickness of only 150 nm to reproduce experimental mass diffusion limitations with maximum current densities of 300 mA/cm^2 (see main text Fig. 4). In contrast, typical diffusion layer thicknesses of 50 μm lead to maximum current densities of 1-10 mA/cm^2. On the electrolyte

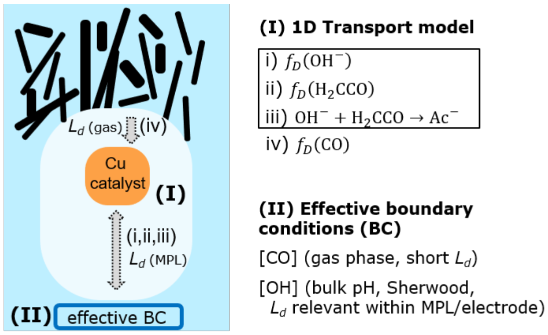

Figure S15: Summary of the effective transport model considered in this work. Diffusion in the solvent and solution reaction within 1 μm of the catalyst surface are solved numerically (i-iii). The boundary conditions of this short diffusion length are given by bulk concentrations and in the case of $\mathrm{OH^-}$ additionally by the Sherwood relation. The latter are decisive to capture the flow cell set up and the following highly alkaline reaction conditions. In contrast to this, the transport of CO is considered separately with an independent diffusion length (iv), representing the gas feed through the GDL. We note that the short diffusion length due to the rapid solution reaction justifies this 1D approximation of transport.

side we consider a diffusion layer thickness of 1 μm for $\mathrm{OH^-}$ and $\mathrm{H_2CCO}$. This diffusion layer thickness suffices for the solution reaction of $\mathrm{H_2CCO}$ and $\mathrm{OH^-}$ to be completed as shown in Fig. 5a in the main text. Beyond this diffusion layer of 1 μm we assume that the electrode surface is reached (c_{MPL} in Fig. S14) or, alternatively, that homogeneous conditions within the electrode are present. Since the concentration of $\mathrm{H_2CCO}$ is virtually zero at this point, its further transport can be ignored. In contrast, the $\mathrm{OH^-}$ transport from the electrode surface to the “bulk” of the flowing electrolyte is further described by the effective Sherwood relation (see Equ. 11 and 12). We note that extending the electrolyte side diffusion layer of 1 μm does not quantitatively influence the $\mathrm{OH^-}$ transport. Only when considering unphysically thick diffusion layers with a thickness of ≥ 500 μm will these have a noticeable effect by increasing the local pH. This is due to the very alkaline conditions (pH of > 13) where the diffusion related $\mathrm{OH^-}$ accumulation does not significantly change the overall $\mathrm{OH^-}$ concentration in comparison to neutral electrolytes.[S26,S36,S39,S41] Naturally, a high local pH is nevertheless reached which is mainly due to the electrolyte flow. As shown in Fig. S16, the convective transport leads to an additional resistance which leads to very high pH at the electrode surface. For simplicity, the effective transport model is summarized in Fig. S15

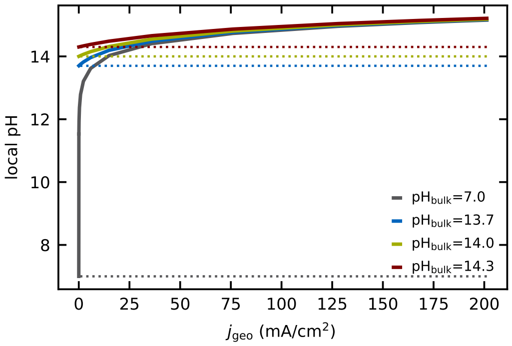

Figure S16: Local pH against geometric current density($j_{geo}^{C_2}$) for different bulk pH as given by the mass-transport relation in Equ. 12. The [OH$^-$] concentration gradient due to the diffusion within the electrode (not included) with an assumed diffusion length of one μm is negligible.

In our multiscale model, we couple the microkinetic and mass transport model via fluxes of CO, OH$^-$ and acetate. In the microkinetic model these are determined by the geometric consumption and production rates of CO and ketene. For the mass transport model, these correspond to the Neumann conditions described in Sec. S5.2. While the fluxes of the microkinetic model serve as input to the mass transport model, the surface concentrations obtained from the mass transport model serve as an input for the microkinetic model. Here we assume for simplicity that the very dilute surface concentration of ketene (compare Fig. S17) is equal to its activity (in the microkinetic model). While this simplification is typical for very dilute solutions, alternatively including a proportionality factor for ketene (i.e. a Henry's law constant) would effectively change the thermodynamic stability of H_2CCO (aq). The Henry's law constant of ketene is unknown, but assuming values of 100-1500 l·atm·mol^{-1}, typical for organic molecules, would lead to a destabilization of 0.12-0.19 eV for H_2CCO (aq). Such an energetic value is contained in the correction we apply to H_2CCO (aq) to reproduce experimental behavior as described in Sec. S5.6.1. The models are then solved iteratively for their respective steady-state until the fluxes (and surface concentrations) align.[S44] The iterative procedure fulfills mass conservation between the microkinetic and transport models due to the consistent boundary conditions. We note that the iterative solution of CO flux leads to negligibly small changes in the surface coverage of $\theta_C O$ since the response through the back reaction of any intermediate after the RDS carries a very low probability.

S5.5 Trends of concentration profiles in the mass transport model

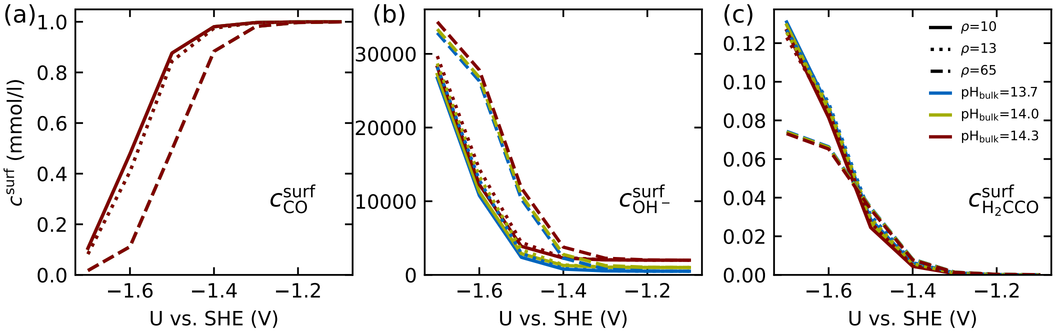

Figure S17: Surface concentrations c_x^{surf} of $x =$ CO (a), $\mathrm{OH^-}$(b), and $\mathrm{H_2CCO}$ (c) against potential for different electrolyte pH and roughness as obtained from our simulations (compare Fig. 4 main text

The mass transport limitations included in our model change the microscopic reaction environment at the catalyst surface. Effectively, the surface concentrations (c^{surf}) of individual species change, in our case of CO, $\mathrm{OH^-}$, and $\mathrm{H_2CCO}$ (see Fig. S17).

Increasing current densities at higher overpotentials or higher roughness give rise to increased concentration gradients. The surface concentrations of reactants (CO) decrease in this case with increasing potential and also with higher roughness, depleting $c^{\mathrm{surf}}_{\mathrm{CO}}$ at the catalyst surface. In contrast, the increasing limitations in transport of products away from the surface at increasing overpotential and corresponding current densities are consistent with the build up in the surface concentrations of the $\mathrm{OH^-}$(aq) and $\mathrm{H_2CCO}$(aq), i.e. of $c^{\mathrm{surf}}_{\mathrm{OH^-}}$ and $c^{\mathrm{surf}}_{\mathrm{H_2CCO}}$ (Figs. S17b,c). With increasing bulk pH $c^{\mathrm{surf}}_{\mathrm{OH^-}}$ increases and $c^{\mathrm{surf}}_{\mathrm{H_2CCO}}$ decreases where the latter is due to the accelerated solution phase reaction. The trends in the $c^{\mathrm{surf}}_{\mathrm{H_2CCO}}$ and $c^{\mathrm{surf}}_{\mathrm{OH^-}}$ with respect to ρ are more nuanced. At low overpotentials, an increased ρ gives a higher production rate of $\mathrm{OH^-}$(aq) and $\mathrm{H_2CCO}$(aq), and consequently *more* build up in both $c^{\mathrm{surf}}_{\mathrm{H_2CCO}}$ and $c^{\mathrm{surf}}_{\mathrm{OH^-}}$. At high overpotentials, where the production of $\mathrm{OH^-}$(aq) and $\mathrm{H_2CCO}$(aq) is limited by CO transport to the surface, the main impact of increasing ρ is a greater rate of $\mathrm{H_2CCO}$ re-adsorption and subsequent production of other $\mathrm{C_2}$ vs. a fixed rate of $\mathrm{H_2CCO}$

transport away, which leads to a change in the steady-state re-adsorption equilibrium. This yields an earlier levelling off with negative potential of $c^{\mathrm{surf}}_{\mathrm{H_2CCO}}$ with increasing ρ.

S5.6 Sensitivity of kinetics to energetics

S5.6.1 (Re-)adsorption energy influences SDS-sol

The acetate selectivity is influenced by mass transport through a combination of diffusion and surface reaction. As indicated in Fig. 2 in the main text, the corresponding selectivity step (labeled SDS-sol) consists of desorbed ketene which can either move towards the electrolyte bulk and react to acetate or (re-)adsorb on the catalyst surface. Central to this SDS-sol is the adsorption rate of ketene to the catalyst surface which scales with the free barrier of adsorption $\Delta G^{\ddagger}_{\mathrm{ads}}$ (see Fig. S14). We compute this barrier using DFT simulations where we determine the transition state by simulating the desorption process (using a CI-NEB search). We do not include an explicit water layer in those barrier calculations as they artificially penalize the barrier on the stepped surfaces. We further determine the free energy of desorbed ketene from its gas-phase energy and add a solvation correction as obtained from the SCCS[S45] implicit solvation scheme of $\Delta G_{\mathrm{solv}} =$ -0.09 eV. For the investigated Cu facets we find different $\Delta G^{\ddagger}_{\mathrm{ads}}$, which dependent on the overall stability of H_2CCO^* and its desorption barrier.

We test the sensitivity of SDS-sol on $\Delta G^{\ddagger}_{\mathrm{ads}}$ in our transport coupled microkinetic model. We thereby systematically vary $\Delta G^{\ddagger}_{\mathrm{ads}}$ at a potential of -1.3 V vs. SHE where SDS-surf does not influence the acetate selectivity of SDS-sol (see main text and Sec. S5.6.2). As shown in Fig. S18, the selectivity is very sensitive to the ketene (re-)adsorption. The indicated experimental selectivity in Fig. S18 coincides with the $\Delta G^{\ddagger}_{\mathrm{ads}}$ of the Cu(211) facet. We note, however, that the typical error of DFT is within 0.1-0.2 eV[S7] whereby also Cu(100) may still be active for the acetate selectivity behavior. We further note, that we do not account for competitive water adsorption or field effects which may further influence the computed desorption barriers[S46–S48] and affect the facet dependence. In the main text we

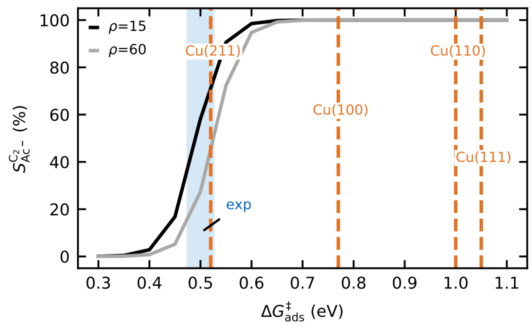

Figure S18: Acetate selectivity among C_2 products ($S_{\mathrm{Ac}^-}^{\mathrm{C}_2}$) against the ketene (re-) adsorption barrier $\Delta G_{\mathrm{ads}}{}^{\ddagger}$ as computed by our transport-coupled microkinetic model for -1.3 V vs. SHE and pH=14 and different roughness (ρ). The blue shaded area marks the selectivities encountered in experiment for equivalent conditions (compare Fig. 4 in the main text). The vertical orange lines present $\Delta G_{\mathrm{ads}}{}^{\ddagger}$ as computed by DFT for the different investigated facets. Taking into account the typical DFT accuracy, Cu(211) or Cu(100) may be active for the ketene adsorption and selectivity process.

use the energetics for Cu(100), which is generally believed to be active for C_2 products,[S49] for our microkinetic model. This is also supported by the fact that our Cu(100) energetics for SDS-surf best coincide for acetate selectivity (while they are prohibitive for Cu(211), see Sec. S5.6.2). For an experiment-like acetate selectivity behavior with $\Delta G_{\mathrm{ads}}^{\ddagger} \approx 0.5$ eV, we need to apply a correction of +0.28 eV to the desorbed H_2CCO (aq). While this correct slightly extends beyond the typical DFT error, it should be noted that this correction includes a missing unknown thermodynamic correction for the ketene solubility (Henry's law constant, see above Sec. S5.4) and that a bulk H_2CCO(aq) may be not adequately describe the molecules stability at the electrochemical double layer. Alternatively, the correction can be interpreted as an adsorption on Cu(211) followed by diffusion to Cu(100).

S5.6.2 Barrier competition influences SDS-surf

At low overpotentials, the desorption process of (re-)adsorbed H_2CCO^* influences another SDS (labeled SDS-surf see main text). Here, the (re-)adsorbed H_2CCO^* can either get further reduced in a PCET reaction or desorb again. These two competing rates directly depend on the free energy barriers of the reduction ($\Delta G_{\mathrm{PCET}}^{\ddagger}$) and desorption ($\Delta G_{\mathrm{des}}^{\ddagger}$). The energy difference between the barriers $\Delta G^{\ddagger}_{\text{PCET}} - \Delta G^{\ddagger}_{\text{des}}$ indicates how SDS-surf influences the selectivity. With a difference of > 0 most H_2CCO will desorb and of < 0 most H_2CCO will get reduced. Since $\Delta G^{\ddagger}_{\text{PCET}}$ is potential dependent, the selectivity around SDS-surf is also potential dependent. Via this potential dependence we can compare our DFT computed values with experiment.

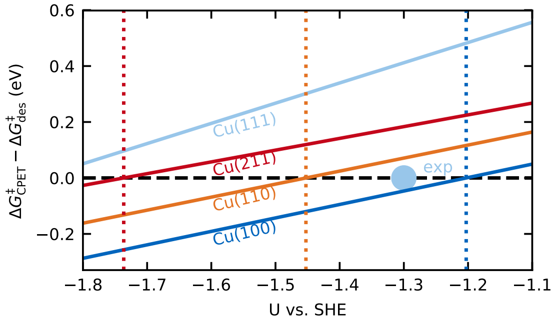

Figure S19: Difference in the lowest reduction $\Delta G^{\ddagger}_{\text{PCET}}$ and desorption $\Delta G^{\ddagger}_{\text{des}}$ barrier of ketene against potential vs. SHE for the investigated Cu facets (compare Tab. S6). The vertical lines indicate when the difference is zero for a certain facet (see colors). At difference $\Delta G^{\ddagger}_{\text{PCET}} - \Delta G^{\ddagger}_{\text{des}} < 0$ the (re-)adsorbed ketene cannot desorb anymore. This situation compromises a minimum in acetate selectivity since all (re-)adsorbed ketene will react to other C_2 products. Experimentally, such a minimum is seen at -1.3 V vs. SHE (compare Fig. 4 in the main text) as indicated by the blue circle. The comparison to experiment clearly points to Cu(100) being active for the acetate selectivity mechanism.

We compare our DFT computed barrier competition for the investigated facets as shown in Fig. S19. At potentials where $\Delta G^{\ddagger}_{\text{PCET}} - \Delta G^{\ddagger}_{\text{des}} = 0$ the acetate selectivity will reach a minimum as all of the (re-)adsorbed H_2CCO^* will get further reduced and cannot desorb (again) to eventually react to acetate. In the experimental data such a selectivity minimum is found around -1.3 V vs. SHE. In Fig. S19, it can be seen that a difference between the free energy barriers $\Delta G^{\ddagger}_{\text{PCET}} - \Delta G^{\ddagger}_{\text{des}} = 0$ close to the experimental potential is only found for Cu(100) and Cu(110). Cu(211) and Cu(111) are considerably further off. The reason why Cu(100) and Cu(110) coincide to experimental values is due to its high $\Delta G^{\ddagger}_{\text{des}}$. Their high barriers are based on a strong interaction of ketene with the Cu surface where the molecule slightly disrupts its conjugated C=C=O bond.

S5.6.3 Acetate selectivity is insensitive to DFT thermodynamics

Apart from the adsorption barrier $\Delta G^{\ddagger}_{\text{ads}}$ (see Sec. S5.6.1), desorption barrier $\Delta G^{\ddagger}_{\text{des}}$, and the protonation energy $\Delta G^{\ddagger}_{\text{PCET}}$ of H_2CCO^* (see Sec. S5.6.2), other DFT derived energies influence the selectivity in our model only marginally. This is due to the fact, that most of these energies affect the kinetics after the RDS and are not critical for any SDS.[S50] Only the adsorption energy of CO(g) yields changes when varying strongly. This is shown in Fig. S20 where we exchanged different reaction free energies according to the investigated facets – leaving only the critical barriers as well as the fitted effective RDS constant as described in Sec. S5.1, S5.6.1, and S5.6.2. Differences in selectivity are seen when the facet dependent $\Delta G^{\text{CO}}_{\text{ads}}$ are present (Fig. S20 left) and fully disappear when adjusted (Fig. S20 right).

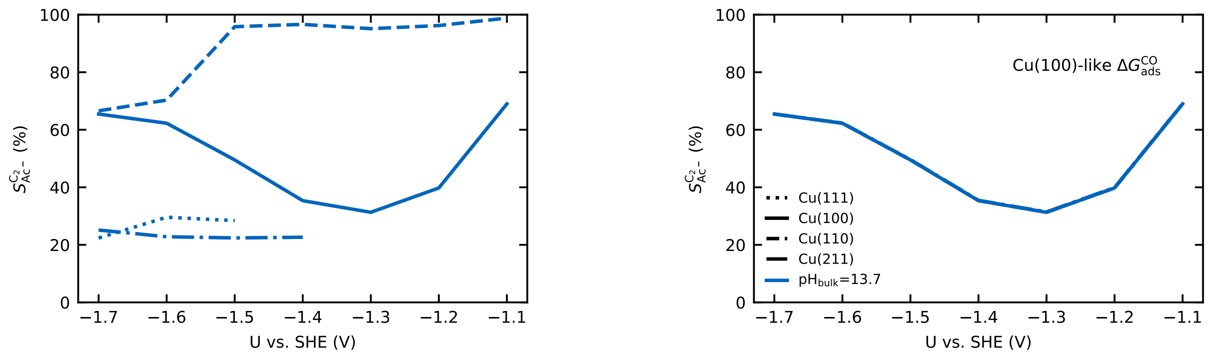

Figure S20: Acetate selectivity among C_2 products ($S^{C_2}_{\text{Ac}^-}$) against U vs. SHE as computed with our transport coupled kinetic model. We exchanged the reaction free energies between the intermediates according to the investigated facets Cu(100), Cu(111), Cu(110), and Cu(211) (compare Sec. S5.1 and Fig. 2 and 3 in the main text). We only left the barrier of the RDS (fitted), reduction, de- and adsorption barrier of H_2CCO^* Cu(100)-like (left). (right) We additionally used a Cu(100)-like CO* adsorption energy ($\Delta G^{\text{CO}}_{\text{ads}}$) for the different simulations with otherwise facet-dependent energies.

As shown in Fig. S20, the CO* adsorption energy ($\Delta G^{\text{CO}}_{\text{ads}}$) leads to changes in selectivity. This is due to the resulting CO* coverage as depicted in Tab. S7. Including the facet dependent $\Delta G^{\text{CO}}_{\text{ads}}$, we find only Cu(100) to give the U-shaped selectivity profile. Cu(110) in contrast demonstrates almost 100 % acetate selectivity since the CO* coverage (θ_{CO}) of 98 % inhibits (re-)adsorption of ketene. Cu(111) and Cu(211) show a diverging behavior with a significantly lowered selectivity due to an overall low coverage and a very high ratio of empty sites (see Tab. S7). The empty sites result in more sites for (re-)adsorption of $H_2CCO(aq)$ which subsequently gets reduced further to other C_2 products, lowering $S^{C_2}_{Ac^-}$. The low coverage on Cu(111) and Cu(211) is due to a weak CO* binding. While for Cu(111) this is inherent to its electronic structure, for Cu(211) this is due to competitive water adsorption. The latter has been predicted by AIMD simulations[S48] and is well captured by the static water layer in our simulations. In our model in the main text we use the Cu(100) CO* adsorption energy which gives $\theta_{CO} \approx 25\%$. This value resembles the coverage usually found when including lateral interactions,[S30] which justifies neglecting them in this model.

Table S7: Share of empty (θ^*) and CO* (θ_{CO}) covered sites in (%) for the simulations with different facet dependent thermodynamics (see text) at a U_{SHE} = -1.4 V.

	Cu(100)	Cu(111)	Cu(110)	Cu(211)
θ^*	74.6	99.9	2.25	99.9
θ_{CO}	25.4	$2.0 \cdot 10^{-4}$	97.7	$2.9 \cdot 10^{-2}$

S6 The pH dependence of the acetate selectivity necessitates a solution reaction

As briefly discussed in the main text ("Alternative pathways are unlikely") we elaborate here in more detail the implication of the pH dependence of the selectivity of acetate in competition to other C_2 products. The acetate selectivity among C_2 products thereby increases with increasing pH ($\frac{dr}{d\text{pH}} > 0$). This trend necessitates a reaction involving OH^- which most likely occurs in solution.

The selectivity between acetate and other C_2 products follows a SDS where one of the two products has an intrinsic pH dependence (see Fig. S21 a). Electrochemical reactions often show a distinct pH dependence since their activity scales with the concentration of proton donors.[S13] This pH dependence is especially true in acidic conditions where H_3O^+

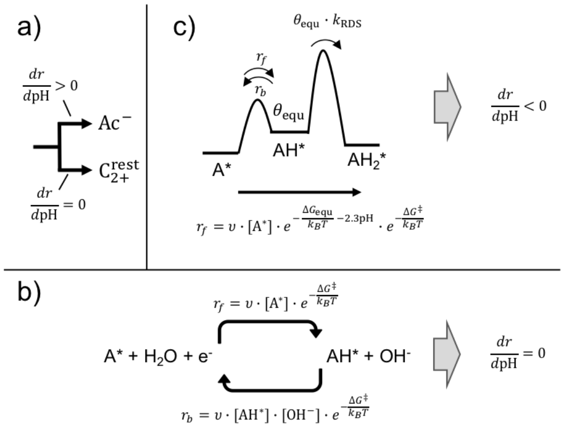

Figure S21: Selectivity trends with pH. a) Phenomenological selectivity behavior between Acetate and other C_2 products (C_2^{rest}). The pH independence of C_2^{rest} is known from the selectivity between C_1 and C_2 products[S28,S29] b) Elementary PCET reaction of an adsorbate A^* in alkaline conditions. Shown is the rate equation for the forward r_f and backward r_b reaction. $\Delta G^\ddagger$ is the activation energy of the governing PCET reaction at a fixed potential vs. SHE, k_B the Boltzmann constant, T the temperature, and $[X]$ is the concentration of the intermediate X c) Possible intrinsic pH effect of two consecutive PCET steps with the second step as the RDS. The first step is pre-equilibrated with equilibrium coverage θ_{equ} which is pH dependent. ΔG_{equ} is the reaction energy for $A^* \rightarrow AH^*$ at a fixed potential vs. SHE.

is the proton donor.[S13] In neutral and alkaline conditions PCET steps depend on H_2O as the proton donor (see Fig. S21 b). Since the concentration of H_2O is independent of pH there is no intrinsic pH dependence ($\frac{dr}{\mathrm{dpH}} = 0$) of PCET steps in alkaline conditions.[S51] It should be noted, that the backward reaction does however depend on OH^- but PCET steps are usually very down hill and therefore their pH dependence matters very little and only at low overpotentials. Furthermore, the pH dependence of C_2 products does not show an inverse pH-activity which means that their RDS is intrinsically independent of pH as well ($\frac{dr}{\mathrm{dpH}} = 0$) which is in contrast to e.g. methane which shows increased activity with decreasing pH ($\frac{dr}{\mathrm{dpH}} < 0$).[S28,S29] It follows that an acetate competition along any step towards the C_2 products, i.e. either the RDS or a PCET step after the RDS, needs to occur with an intrinsic positive pH dependence (increasing activity with increasing pH, $\frac{dr}{\mathrm{dpH}} > 0$) as depicted in Fig. S21.

Naturally, there are pH dependent electrochemical reactions in CORR at alkaline conditions evident in the Nernst-like shifts of C_1 products. These, however, require a pre-equilibrium which is pH dependent before the rate determining step as shown in Fig. S21 c. The first step thereby needs to be a PCET step, which will lead to a pH dependent coverage preceding the RDS. In reduction reactions this pre-equilibrium can, however, only have an increasing coverage and therefore activity with decreasing pH. This yields an instrinsic negative pH dependence ($\frac{dr}{d\mathrm{pH}} < 0$) which is opposite to the one required for acetate. It follows that the only way we obtain an intrinsic positive pH dependence ($\frac{dr}{d\mathrm{pH}} > 0$) is via the involvement of OH^- in the forward reaction.

A reaction involving OH^- is a nucleophilic attack which unlikely occurs on a negatively charged surface. For instance OH^- is known to deplete at the immediate catalyst surface due to migration.[S36] A solution reaction is therefore most likely. Since the solution reaction of ketene to acetate via OH^- is well known[S24] we assume this to be the relevant SDS towards acetate. With this SDS, acetate and other C_2 products would necessarily share the same RDS, which fits to experimental observations as further elaborated in the main text.

S7 Analytical derivation of acetate selectivity through ketene hydrolysis

S7.1 Analytical derivation of diffusion-reaction system for ketene hydrolysis

In the following we derive an analytical expression for the 1-dimensional diffusion of ketene (H_2CCO) from a source and its simultaneous hydrolysis at steady-state. The flux of ketene $\frac{d[\mathrm{H_2CCO}]}{dt}$ along the catalyst surface normal x in steady state can be described as

$$\frac{d[\mathrm{H_2CCO}]}{dt} = D_{\mathrm{H_2CCO}} \frac{d^2[\mathrm{H_2CCO}]}{dx^2} - k_{\mathrm{sol}}[\mathrm{OH^-}][\mathrm{H_2CCO}] = 0 \tag{22}$$

where $[H_2CCO]$ and $[OH^-]$ is the concentration of species ketene and hydroxide along x, respectively and D_{H_2CCO} the diffusion coefficient of ketene. In comparison to Equ. 10, the flux is defined as propagating away from a source (the catalyst) to describe the diffusion of ketene and its consumption in the chemical reaction as two opposing processes.[S52] A necessary approximation is a constant concentration of hydroxide

$$[\mathrm{OH^-}] = [\mathrm{OH^-}]^{\mathrm{bulk}} \tag{23}$$

in order to circumvent the interdependence of $[OH^-]$ and $[H_2CCO]$ which we would need to solve numerically (as we do in our transport model). This approximation is, however, justified in alkaline conditions since $[OH^-] >> [H_2CCO]$ and the consumption of OH^- is marginal to its overall concentration. The ketene concentration is only about few μmol, as shown in Fig. 5 in the main text, and therefore several order of magnitude lower than OH^- down to a pH of 10. We note that with the approximation of a constant concentration of OH^- a dependence on its diffusion coefficient drops out.

We solve the remaining homogeneous ordinary differential equation 22 by re-arranging it to

$$\frac{d^2[\mathrm{H_2CCO}]}{dx^2} = \frac{k_{\mathrm{sol}}[\mathrm{OH^-}]^{\mathrm{bulk}}}{D_{\mathrm{H_2CCO}}}[\mathrm{H_2CCO}] \tag{24}$$

which allows us to identify a general solution. From the functional form $f'' = kf$ we propose an exponential function $f = e^{rt}$ as the Ansatz. By substituting $[H_2CCO]$ for f, we obtain

$$\begin{aligned}
D_{\mathrm{H_2CCO}}\, f'' - k_{\mathrm{sol}}[\mathrm{OH^-}]^{\mathrm{bulk}} f &= 0 \\
D_{\mathrm{H_2CCO}}\, r^2 e^{rt} - k_{\mathrm{sol}}[\mathrm{OH^-}]^{\mathrm{bulk}} e^{rt} &= 0 \\
e^{rt}(D_{\mathrm{H_2CCO}}\, r^2 - k_{\mathrm{sol}}[\mathrm{OH^-}]^{\mathrm{bulk}}) &= 0
\end{aligned} \tag{25}$$

where $(D_{\mathrm{H_2CCO}}\, r^2 - k_{\mathrm{sol}}[\mathrm{OH^-}]^{\mathrm{bulk}}) = 0$ is the characteristic polynomial from which we obtain

$$r^2 = \frac{k_{\mathrm{sol}}[\mathrm{OH^-}]^{\mathrm{bulk}}}{D_{\mathrm{H_2CCO}}} \quad \rightarrow \quad r = \pm\sqrt{\frac{k_{\mathrm{sol}}[\mathrm{OH^-}]^{\mathrm{bulk}}}{D_{\mathrm{H_2CCO}}}} \tag{26}$$

it follows for $[\mathrm{H_2CCO}]$

$$[\mathrm{H_2CCO}] = C_1 e^{\sqrt{\frac{k_{\mathrm{sol}}[\mathrm{OH^-}]^{\mathrm{bulk}}}{D_{\mathrm{H_2CCO}}}}x} + C_2 e^{-\sqrt{\frac{k_{\mathrm{sol}}[\mathrm{OH^-}]^{\mathrm{bulk}}}{D_{\mathrm{H_2CCO}}}}x} \tag{27}$$

where C_1 and C_2 are unknown constants which we solve via boundary conditions. These are:

1. eventually all ketene hydrolyzes leading to $\lim_{x\to\infty}[\mathrm{H_2CCO}] = 0$
2. the concentration of ketene just at the catalyst surface is $[\mathrm{H_2CCO}](x = 0) = [\mathrm{H_2CCO}]_{\mathrm{surf}}$

based on 1. we find that $C_1 = 0$ as Equ. 27 would otherwise diverge to ∞ and it results that $C_2 = [\mathrm{H_2CCO}]_0$ leading to

$$[\mathrm{H_2CCO}] = [\mathrm{H_2CCO}]_{\mathrm{surf}} \cdot e^{-\sqrt{\frac{k_{\mathrm{sol}}[\mathrm{OH^-}]^{\mathrm{bulk}}}{D_{\mathrm{H_2CCO}}}}x} \tag{28}$$

which finally describes the concentration profile of Ketene along the surface normal of the catalyst.

In order to obtain the acetate ($\mathrm{Ac^-}$) flux we integrate $[\mathrm{H_2CCO}] \cdot k_{\mathrm{sol}}[\mathrm{OH^-}]^{\mathrm{bulk}}$ along the surface normal (compare Sec. S5.2).

$$\begin{aligned}\frac{d[\mathrm{Ac^-}]}{dt} &= \int_0^\infty k_{\mathrm{sol}} \cdot [\mathrm{OH^-}]^{\mathrm{bulk}} \cdot [\mathrm{H_2CCO}]dx \\ &= \int_0^\infty k_{\mathrm{sol}} \cdot [\mathrm{OH^-}]^{\mathrm{bulk}} \cdot [\mathrm{H_2CCO}]_{\mathrm{surf}} \cdot e^{-\sqrt{\frac{k_{\mathrm{sol}}[\mathrm{OH^-}]^{\mathrm{bulk}}}{D_{\mathrm{H_2CCO}}}}x} dx\end{aligned} \tag{29}$$

solving the integral within the bounds finally gives

$$\frac{d[\mathrm{Ac^-}]}{dt} = [\mathrm{H_2CCO}]_{\mathrm{surf}} \cdot \sqrt{D_{\mathrm{H_2CCO}} \cdot k_{\mathrm{sol}} \cdot [\mathrm{OH^-}]^{\mathrm{bulk}}} \tag{30}$$

To verify our analytical result we compare the expected ketene profile of Equ. 28 using our finite difference solver assuming a constant $[\mathrm{OH}^-]^{\mathrm{bulk}}$ at pH 13, a boundary condition of $\frac{d[\mathrm{Ac}^-]}{dt} = \frac{d[\mathrm{H_2CCO}]}{dt} = 300\ \mathrm{mA/cm^2}$ acetate partial current density and experimental $D_{\mathrm{H_2CCO}}$[S37] and k_{sol}.[S24] As shown in Fig. S22, the profiles obtain analytically and numerically are almost identical, minute differences are based on the grid spacing of the finite element solver.

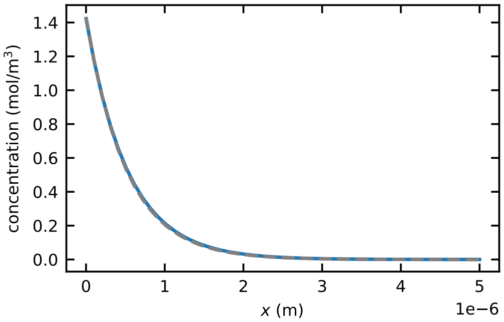

Figure S22: Concentration profile of ketene against the surface normal of the catalyst x. The concentration profile is solved via a finite difference solver (blue line) and analytically (grey dashed line) using Equ. 28 and 30 as further described in the text.

S7.2 Analytical expression for acetate selectivity

We can use the expression in Equ. 30 to evaluate the selectivity for acetate among the other $\mathrm{C_2}$ products ($S^{\mathrm{C_2}}_{\mathrm{Ac^-}}$) at the selectivity determining step in the conversion of ketene $\mathrm{H_2CCO(aq)}$ (SDS-sol, see Fig. 3 main text). The selectivity follows:

$$S^{\mathrm{C_2}}_{\mathrm{Ac^-}} = \frac{f_{\mathrm{Ac^-}}}{f^{\mathrm{ads}}_{\mathrm{H_2CCO}} + f_{\mathrm{Ac^-}}} = \frac{1}{\left(R^{\mathrm{C_2}}_{\mathrm{Ac^-}}\right)^{-1} + 1} \tag{31}$$

where $f_{\mathrm{Ac^-}}$ is the flux of acetate ($= \frac{d[\mathrm{Ac}^-]}{dt}$), $f^{\mathrm{ads}}_{\mathrm{H_2CCO}}$ the flux of ketene adsorption and $R^{\mathrm{C_2}}_{\mathrm{Ac^-}}$ is the ratio $\frac{f_{\mathrm{Ac^-}}}{f^{\mathrm{ads}}_{\mathrm{H_2CCO}}}$ closely related to $S^{\mathrm{C_2}}_{\mathrm{Ac^-}}$. For $R^{\mathrm{C_2}}_{\mathrm{Ac^-}}$ we can derive the following expression inserting Equ. 30 for $f_{\mathrm{Ac^-}}$:

$$R^{\mathrm{C_2}}_{\mathrm{Ac^-}} = \frac{f_{\mathrm{Ac^-}}}{f^{\mathrm{ads}}_{\mathrm{H_2CCO}}} = \frac{[\mathrm{H_2CCO}]_{\mathrm{surf}} \cdot \sqrt{D_{\mathrm{H_2CCO}} \cdot [[\mathrm{OH^-}]_{\mathrm{surf}} \cdot k_{\mathrm{sol}}}}{\rho \cdot [\mathrm{H_2CCO}]_{\mathrm{surf}} \cdot \theta^* \cdot k^{\mathrm{ads}}_{\mathrm{H_2CCO}}} = \frac{\sqrt{D_{\mathrm{H_2CCO}} \cdot [\mathrm{OH^-}]_{\mathrm{surf}} \cdot k_{\mathrm{sol}}}}{\rho \cdot \theta^* \cdot k^{\mathrm{ads}}_{\mathrm{H_2CCO}}} \tag{32}$$

where $f^{\mathrm{ads}}_{\mathrm{H_2CCO}}$ was substituted for the rate of ketene adsorption which is proportional to the surface concentration of ketene $[\mathrm{H_2CCO}]_{\mathrm{surf}}$ the amount of free sites θ^* and the adsorption rate constant $k^{\mathrm{ads}}_{\mathrm{H_2CCO}}$. The roughness $\rho(= \frac{A_{\mathrm{ECSA}}}{A_{\mathrm{Geo}}}$ scales the catalyst surface (A_{ECSA}) dependent process $f^{\mathrm{ads}}_{\mathrm{H_2CCO}}$ to the transport related process $f_{\mathrm{Ac^-}}$.

Equ. 32 captures the acetate selectivity trends with respect to ρ and pH, and shows that other decisive factors determining acetate selectivity are the H_2CCO diffusion, the rate of the solution reaction, and the (re-)adsorption rate of H_2CCO. Both $f_{\mathrm{Ac^-}}$ and $f_{\mathrm{C_2}}$ have a first order dependence on $[\mathrm{H_2CCO}]_{\mathrm{surf}}$. Therefore, acetate selectivity has no net dependence on the ketene surface concentration. With no dependence on the latter and no potential dependent barriers, the only potential dependence in SDS-sol results from the local pH ($[\mathrm{OH^-}]_{\mathrm{surf}}$). This constitutes the main potential dependence at high overpotentials (see main text Fig. 4). The square-root dependence of $[\mathrm{OH^-}]_{\mathrm{surf}}$ scales weaker than the linear dependence of ρ which explains why an increase in ρ does not cancel with an increase in $[\mathrm{OH^-}]_{\mathrm{surf}}$ due to the accompanied change in local pH at high current densities.

References

(S1) Jouny, M.; Luc, W.; Jiao, F. High-rate electroreduction of carbon monoxide to multi-carbon products. *Nat. Catal.* **2018**, *1*, 748–755.

(S2) Luc, W.; Fu, X.; Shi, J.; Lv, J.-J.; Jouny, M.; Ko, B. H.; Xu, Y.; Tu, Q.; Hu, X.; Wu, J.; Yue, Q.; Jiao, F.; Kang, Y. Two-dimensional copper nanosheets for electrochemical reduction of carbon monoxide to acetate. *Nat. Catal.* **2019**, *2*, 423–430.

(S3) Ripatti, D. S.; Veltman, T. R.; Kanan, M. W. Carbon monoxide gas diffusion electrolysis that produces concentrated C2 products with high single-pass conversion. *Joule* **2019**, *3*, 240–256.

(S4) (a) Bertheussen, E.; Verdaguer-Casadevall, A.; Ravasio, D.; Montoya, J. H.; Trimarco, D. B.; Roy, C.; Meier, S.; Wendland, J.; Nørskov, J. K.; Stephens, I. E.; Chorkendorff, I. Acetaldehyde as an intermediate in the electroreduction of carbon monoxide to ethanol on oxide-derived copper. *Angew. Chem. Int. Ed.* **2016**, *128*, 1472–1476; (b) Bertheussen, E.; Hogg, T. V.; Abghoui, Y.; Engstfeld, A. K.; Chorkendorff, I.; Stephens, I. E. Electroreduction of CO on polycrystalline copper at low overpotentials. *ACS Energy Lett.* **2018**, *3*, 634–640; (c) Zhang, W.; Qin, Q.; Dai, L.; Qin, R.; Zhao, X.; Chen, X.; Ou, D.; Chen, J.; Chuong, T. T.; Wu, B.; Zheng, N. Electrochemical reduction of carbon dioxide to methanol on hierarchical Pd/SnO2 nanosheets with abundant Pd–O–Sn interfaces. *Angew. Chem. Int. Ed.* **2018**, *57*, 9475–9479; (d) Wang, L.; Nitopi, S. A.; Bertheussen, E.; Orazov, M.; Morales-Guio, C. G.; Liu, X.; Higgins, D. C.; Chan, K.; Nørskov, J. K.; Hahn, C.; Jaramillo, T. F. Electrochemical carbon monoxide reduction on polycrystalline copper: Effects of potential, pressure, and pH on selectivity toward multicarbon and oxygenated products. *ACS Catal.* **2018**, *8*, 7445–7454; (e) Wang, L.; Nitopi, S.; Wong, A. B.; Snider, J. L.; Nielander, A. C.; Morales-Guio, C. G.; Orazov, M.; Higgins, D. C.; Hahn, C.; Jaramillo, T. F. Electrochemically converting carbon monoxide to liquid fuels by directing selectivity with electrode surface area. *Nat. Catal.* **2019**, *2*, 702–708; (f) Raciti, D.; Cao, L.; Livi, K. J.; Rottmann, P. F.; Tang, X.; Li, C.; Hicks, Z.; Bowen, K. H.; Hemker, K. J.; Mueller, T.; Wang, C. Low-overpotential electroreduction of carbon monoxide using copper nanowires. *ACS Catal.* **2017**, *7*, 4467–4472.

(S5) Mortensen, J. J.; Hansen, L. B.; Jacobsen, K. W. Real-space grid implementation of the projector augmented wave method. *Phys. Rev. B* **2005**, *71*, 035109.

(S6) Enkovaara, J.; Rostgaard, C.; Mortensen, J. J.; Chen, J.; Dułak, M.; Ferrighi, L.;

Gavnholt, J.; Glinsvad, C.; Haikola, V.; Hansen, H. A.; Kristoffersen, H. H.; Kuisma, M.; Larsen, A. H.; Lehtovaara, L.; Ljungberg, M.; Lopez-Acevedo, O.; Moses, P. G.; Ojanen, J.; Olsen, T.; Petzold, V.; Romero, N. A.; Stausholm-Møller, J.; Strange, M.; Tritsaris, G. A.; Vanin, M.; Walter, M.; Hammer, B.; Häkkinen, H.; Madsen, G. K. H.; Nieminen, R. M.; Nørskov, J. K.; Puska, M.; Rantala, T. T.; Schiøtz, J.; Thygesen, K. S.; Jacobsen, K. W. Electronic structure calculations with GPAW: a real-space implementation of the projector augmented-wave method. *J. Phys.: Condens. Matter* **2010**, *22*, 253202.

(S7) Wellendorff, J.; Lundgaard, K. T.; Møgelhøj, A.; Petzold, V.; Landis, D. D.; Nørskov, J. K.; Bligaard, T.; Jacobsen, K. W. Density functionals for surface science: Exchange-correlation model development with Bayesian error estimation. *Phys. Rev. B* **2012**, *85*, 235149.

(S8) Held, A.; Walter, M. Simplified continuum solvent model with a smooth cavity based on volumetric data. *J. Chem. Phys.* **2014**, *141*, 174108.

(S9) Bondi, A. v. van der Waals volumes and radii. *J. Phys. Chem.* **1964**, *68*, 441–451.

(S10) Kastlunger, G.; Lindgren, P.; Peterson, A. A. Controlled-potential simulation of elementary electrochemical reactions: Proton discharge on metal surfaces. *J. Phys. Chem. C* **2018**, *122*, 12771–12781.

(S11) Nørskov, J.; Rossmeisl, J.; Logadottir, A.; Lindqvist, L.; Kitchin, J.; Bligaard, T.; Jónsson, H. Origin of the Overpotential for Oxygen Reduction at a Fuel-Cell Cathode. *J. Phys. Chem. B* **2004**, *108*, 17886–17892.

(S12) Christensen, R.; Hansen, H. A.; Vegge, T. Identifying systematic DFT errors in catalytic reactions. *Catal. Sci. Technol.* **2015**, *5*, 4946–4949.

(S13) Nørskov, J. K.; Studt, F.; Abild-Pedersen, F.; Bligaard, T. *Fundamental Concepts in Heterogeneous Catalysis*; John Wiley & Sons, Inc., 2014.

(S14) Boes, J. R.; Mamun, O.; Winther, K.; Bligaard, T. Graph Theory Approach to High-Throughput Surface Adsorption Structure Generation. *J. Phys. Chem. A* **2019**, *123*, 2281–2285.

(S15) Monkhorst, H.; Pack, J. Special Points for Brillouin-Zone Integrations. *Phys. Rev. B: Condens. Matter.* **1976**, *13*, 5188–5192.

(S16) Lindgren, P.; Kastlunger, G.; Peterson, A. A. Scaled and Dynamic Optimizations of Nudged Elastic Bands. *Journal of chemical theory and computation* **2019**, *15*, 5787–5793.

(S17) Larsen, A. H.; Mortensen, J. J.; Blomqvist, J.; Castelli, I. E.; Christensen, R.; Dułak, M.; Friis, J.; Groves, M. N.; Hammer, B.; Hargus, C.; Hermes, E. D.; Jennings, P. C.; Jensen, P. B.; Kermode, J.; Kitchin, J. R.; Kolsbjerg, E. L.; Kubal, J.; Kaasbjerg, K.; Lysgaard, S.; Maronsson, J. B.; Maxson, T.; Olsen, T.; Pastewka, L.; Peterson, A.; Rostgaard, C.; Schiøtz, J.; Schütt, O.; Strange, M.; Thygesen, K. S.; Vegge, T.; Vilhelmsen, L.; Walter, M.; Zeng, Z.; Jacobsen, K. W. The atomic simulation environment—a Python library for working with atoms. *J. Phys. Condens. Matter* **2017**, *29*, 273002.

(S18) Lindgren, P.; Kastlunger, G.; Peterson, A. A. A Challenge to the G 0 Interpretation of Hydrogen Evolution. *ACS Catal.* **2019**, *10*, 121–128.

(S19) Gauthier, J. A.; Ringe, S.; Dickens, C. F.; Garza, A. J.; Bell, A. T.; Head-Gordon, M.; Nørskov, J. K.; Chan, K. Challenges in modeling electrochemical reaction energetics with polarizable continuum models. *ACS Catal.* **2018**, *9*, 920–931.

(S20) Gauthier, J. A.; Dickens, C. F.; Heenen, H. H.; Vijay, S.; Ringe, S.; Chan, K. Unified approach to implicit and explicit solvent simulations of electrochemical reaction energetics. *Journal of chemical theory and computation* **2019**, *15*, 6895–6906.

(S21) De Gregorio, G. L.; Burdyny, T.; Loiudice, A.; Iyengar, P.; Smith, W. A.; Buonsanti, R. Facet-dependent selectivity of Cu catalysts in electrochemical CO2 reduction at commercially viable current densities. *ACS Catal.* **2020**, *10*, 4854–4862.

(S22) Wang, Y.; Shen, H.; Livi, K. J.; Raciti, D.; Zong, H.; Gregg, J.; Onadeko, M.; Wan, Y.; Watson, A.; Wang, C. Copper nanocubes for CO_2 reduction in gas diffusion electrodes. *Nano Lett.* **2019**, *19*, 8461–8468.

(S23) Jouny, M.; Lv, J.-J.; Cheng, T.; Ko, B. H.; Zhu, J.-J.; Goddard, W. A.; Jiao, F. Formation of carbon–nitrogen bonds in carbon monoxide electrolysis. *Nat. Chem.* **2019**, *11*, 846–851.

(S24) Andraos, J.; Kresge, A. J. Correlation of rates of uncatalyzed and hydroxide-ion catalyzed ketene hydration. A mechanistic application and solvent isotope effects on the uncatalyzed reaction. *Can. J. Chem.* **2000**, *78*, 508–515.

(S25) Modestino, M. A.; Hashemi, S. M. H.; Haussener, S. Mass transport aspects of electrochemical solar-hydrogen generation. *Energy Environ. Sci.* **2016**, *9*, 1533–1551.

(S26) Burdyny, T.; Smith, W. A. CO_2 reduction on gas-diffusion electrodes and why catalytic performance must be assessed at commercially-relevant conditions. *Energy Environ. Sci.* **2019**, *12*, 1442–1453.

(S27) Virtanen, P.; Gommers, R.; Oliphant, T. E.; Haberland, M.; Reddy, T.; Cournapeau, D.; Burovski, E.; Peterson, P.; Weckesser, W.; Bright, J.; van der Walt, S. J.; Brett, M.; Wilson, J.; Millman, K. J.; Mayorov, N.; Nelson, A. R. J.; Jones, E.; Kern, R.; Larson, E.; Carey, C. J.; Polat, I.; Feng, Y.; Moore, E. W.; VanderPlas, J.; Laxalde, D.; Perktold, J.; Cimrman, R.; Henriksen, I.; Quintero, E. A.; Harris, C. R.; Archibald, A. M.; Ribeiro, A. H.; Pedregosa, F.; van Mulbregt, P. SciPy 1.0: fundamental algorithms for scientific computing in Python. *Nature methods* **2020**, *17*, 261–272.

(S28) Nitopi, S.; Bertheussen, E.; Scott, S. B.; Liu, X.; Engstfeld, A. K.; Horch, S.; Seger, B.; Stephens, I. E.; Chan, K.; Hahn, C.; Nørskov, J.; Jaramillo, T. F.; Chorkendorff, I. Progress and perspectives of electrochemical CO2 reduction on copper in aqueous electrolyte. *Chem. Rev.* **2019**, *119*, 7610–7672.

(S29) Liu, X.; Schlexer, P.; Xiao, J.; Ji, Y.; Wang, L.; Sandberg, R. B.; Tang, M.; Brown, K. S.; Peng, H.; Ringe, S.; Hahn, C.; Jaramillo, T. F.; Nørskov, J. K.; Chan, K. pH effects on the electrochemical reduction of $CO(_2)$ towards C_2 products on stepped copper. *Nat. Commun.* **2019**, *10*.

(S30) Lausche, Adam C. and Medford, Andrew J. and Kahn, Tuhin Suvra and Xu, Yue and Bligaard, Thomas and Abild-Pedersen, Frank and Nørskov, Jens K. and Studt, Felix, On the effect of coverage-dependent adsorbate–adsorbate interactions for CO methanation on transition metal surfaces. *J. Catal.* **2013**, *307*, 275–282.

(S31) Kas, R.; Yang, K.; Bohra, D.; Kortlever, R.; Burdyny, T.; Smith, W. A. Electrochemical CO_2 reduction on nanostructured metal electrodes: fact or defect? *Chem. Sci.* **2020**, *11*, 1738–1749.

(S32) Newman, J.; Thomas-Alyea, K. *Electrochemical Systems*, 3rd ed.; Wiley-Interscience, 2004.

(S33) Subramaniam, A.; Chen, J.; Jang, T.; Geise, N. R.; Kasse, R. M.; Toney, M. F.; Subramanian, V. R. Analysis and simulation of one-dimensional transport models for lithium symmetric cells. *J. Electrochem. Soc.* **2019**, *166*, A3806.

(S34) Heenen, H. H.; Voss, J.; Scheurer, C.; Reuter, K.; Luntz, A. C. Multi-ion conduction in Li3OCl glass electrolytes. *Journal Phys. Chem. Lett.* **2019**, *10*, 2264–2269.

(S35) Cussler, E. L.; Cussler, E. L. *Diffusion: mass transfer in fluid systems*; Cambridge university press, 2009.

(S36) Bohra, D.; Chaudhry, J. H.; Burdyny, T.; Pidko, E. A.; Smith, W. A. Modeling the electrical double layer to understand the reaction environment in a CO2 electrocatalytic system. *Energy Environ. Sci.* **2019**, *12*, 3380–3389.

(S37) Gharagheizi, F. Determination of diffusion coefficient of organic compounds in water using a simple molecular-based method. *Ind. Eng. Chem. Res* **2012**, *51*, 2797–2803.

(S38) Weng, L.-C.; Bell, A. T.; Weber, A. Z. Modeling gas-diffusion electrodes for CO_2 reduction. *Phys. Chem. Chem. Phys.* **2018**, *20*, 16973–16984.

(S39) Suter, S.; Haussener, S. Optimizing mesostructured silver catalysts for selective carbon dioxide conversion into fuels. *Energy Environ. Sci.* **2019**, *12*, 1668–1678.

(S40) Sander, R. Compilation of Henry's law constants (version 4.0) for water as solvent. *Atmos. Chem. Phys* **2015**, *15*, 4399–4981.

(S41) Bohra, D.; Chaudhry, J.; Burdyny, T.; Pidko, E.; Smith, W. Mass Transport in Catalytic Pores of GDE-Based CO2 Electroreduction Systems. **2020**,

(S42) Bird, B. R.; Stewart, W. E.; N, L. E. *Transport Phenomena*; John Wiley & Sons, Inc., 2002.

(S43) COMSOL AB, S., Stockholm COMSOL Multiphysics ®. `www.comsol.com`.

(S44) Ringe, S.; Morales-Guio, C. G.; Chen, L. D.; Fields, M.; Jaramillo, T. F.; Hahn, C.; Chan, K. Double layer charging driven carbon dioxide adsorption limits the rate of electrochemical carbon dioxide reduction on Gold. *Nat. Commun.* **2020**, *11*, 1–11.

(S45) Andreussi, O.; Dabo, I.; Marzari, N. Revised self-consistent continuum solvation in electronic-structure calculations. *J. Chem. Phys.* **2012**, *136*, 064102.

(S46) Montoya, J. H.; Shi, C.; Chan, K.; Nørskov, J. K. Theoretical insights into a CO dimerization mechanism in CO2 electroreduction. *J. Phys. Chem. Lett.* **2015**, *6*, 2032–2037.

(S47) Resasco, J.; Chen, L. D.; Clark, E.; Tsai, C.; Hahn, C.; Jaramillo, T. F.; Chan, K.; Bell, A. T. Promoter effects of alkali metal cations on the electrochemical reduction of carbon dioxide. *J. Am. Chem. Soc.* **2017**, *139*, 11277–11287.

(S48) Heenen, H. H.; Gauthier, J. A.; Kristoffersen, H. H.; Ludwig, T.; Chan, K. Solvation at metal/water interfaces: An ab initio molecular dynamics benchmark of common computational approaches. *J. Chem. Phys.* **2020**, *152*, 144703.

(S49) Schouten, K. J. P.; Pérez Gallent, E.; Koper, M. T. Structure sensitivity of the electrochemical reduction of carbon monoxide on copper single crystals. *ACS Catal.* **2013**, *3*, 1292–1295.

(S50) Mao, Z.; Campbell, C. T. Apparent activation energies in complex reaction mechanisms: a simple relationship via degrees of rate control. *ACS Catal.* **2019**, *9*, 9465–9473.

(S51) Strmcnik, D.; Uchimura, M.; Wang, C.; Subbaraman, R.; Danilovic, N.; Van Der Vliet, D.; Paulikas, A. P.; Stamenkovic, V. R.; Markovic, N. M. Improving the hydrogen oxidation reaction rate by promotion of hydroxyl adsorption. *Nat. Chem.* **2013**, *5*, 300.

(S52) Kolmogorov, A.; Petrovskii, I.; Piskunov, N. Study of a diffusion equation that is related to the growth of a quality of matter, and its application to a biological problem. *Byul. Mosk. Gos. Univ. Ser. A Mat. Mekh* **1937**, *1*, 26.